Single cell transcriptome analysis defines novel heterogeneity within the pancreatic ductal tree

Audrey M. Hendley[1], Arjun A. Rao[2,3,13], Laura Leonhardt[1,13], Sudipta Ashe[1,13], Jennifer A. Smith[1], Simone Giacometti[1], Xianlu L Peng[4,5], Honglin Jiang[6], David I. Berrios[1], Mathias Pawlak[7], Lucia Y. Li[1], Jonghyun Lee[1], Eric A. Collisson[6], Mark Anderson[1], Gabriela K. Fragiadakis[2,3,8], Jen Jen Yeh[4,5,9], Jimmie Ye Chun[10], Grace E. Kim[11], Valerie M. Weaver[12], and Matthias Hebrok[1]

Correspondence: Matthias.Hebrok@ucsf.edu

Keywords and phrases: scRNA-seq, *Gmnn*, *Spp1*, pancreatic duct ligation, duct heterogeneity

[1]Diabetes Center, University of California, San Francisco, San Francisco, California, USA.
[2]CoLabs, University of California, San Francisco, California, USA.
[3]Bakar ImmunoX Initiative, University of California, San Francisco, California, USA.
[4]Department of Pharmacology, University of North Carolina at Chapel Hill, Chapel Hill, North Carolina, USA.
[5]Lineberger Comprehensive Cancer Center, University of North Carolina at Chapel Hill, Chapel Hill, North Carolina, USA.
[6]Division of Hematology and Oncology, Department of Medicine and Helen Diller Family Comprehensive Cancer Center, UCSF, San Francisco, California, USA.
[7]Evergrande Center for Immunologic Diseases, Harvard Medical School and Brigham and Women's Hospital, Boston, Massachusetts, USA.
[8]Department of Medicine, Division of Rheumatology, University of California, San Francisco, California, USA.
[9]Department of Surgery, University of North Carolina at Chapel Hill, Chapel Hill, North Carolina, USA.
[10]Parker Institute for Cancer Immunotherapy, San Francisco, California, USA.
[11]Department of Pathology, University of California, San Francisco, San Francisco, California, USA.
[12]Center for Bioengineering and Tissue Regeneration, UCSF, San Francisco, California, USA.
[13]These authors contributed equally.

ABSTRACT

Lineage tracing using genetically engineered mouse models is an essential tool for investigating cell-fate decisions of progenitor cells and biology of mature cell types, with relevance to physiology and disease progression. To study disease development, an inventory of an organ's cell types and understanding of physiologic function is paramount. Here, we performed single-cell RNA sequencing to examine heterogeneity of murine pancreatic duct cells, pancreatobiliary cells, and intrapancreatic bile duct cells. We isolated duct cells within the murine pancreas using a *Dolichos biflorus* agglutinin (DBA) lectin sorting strategy that labels all pancreatic duct cell types. Our data suggested the substructure of murine pancreatic duct cells is compartmentalized into three subpopulations. We describe an epithelial-mesenchymal transitory axis in our three pancreatic duct subpopulations and identify *SPP1* as a regulator of this fate decision as well as human duct cell de-differentiation. Our results further identify functional heterogeneity within pancreatic duct subpopulations by elucidating a role for Geminin in accumulation of DNA damage in the setting of chronic pancreatitis. Our findings implicate diverse functional roles for subpopulations of pancreatic duct cells in maintenance of duct cell identity and disease progression and establish a comprehensive road map of murine pancreatic duct cell, pancreatobiliary cell, and intrapancreatic bile duct cell homeostasis.

SIGNIFICANCE

Murine models are extensively used for pancreatic lineage tracing experiments and investigation of pancreatic disease progression. Here, we describe the transcriptome of murine pancreatic duct cells, intrapancreatic bile duct cells, and pancreatobiliary cells at single cell resolution. Our analysis defines novel heterogeneity within the pancreatic ductal tree and supports the paradigm that more than one population of pancreatic duct cells harbors progenitor capacity. We identify and validate unique functional properties of subpopulations of pancreatic duct cells including an epithelial-mesenchymal transcriptomic axis and roles in chronic pancreatic inflammation.

INTRODUCTION

Pancreatic duct cells, while a minority of the composition of the pancreas, play an integral role in secretion and transport of digestive fluid containing proenzymes synthesized by acinar cells, electrolytes, mucins, and bicarbonate. They can serve as a cell of origin for pancreatic ductal adenocarcinoma (PDA) (1, 2) and have been implicated in the pathophysiology of multiple other diseases including cystic fibrosis (3) and pancreatitis (4).

Heterogeneity of a cell type becomes increasingly important in the context of disease and regeneration since different subpopulations can be the driving forces behind pathogenesis. The function of exocrine pancreatic cells is required for survival, yet these cells exhibit limited regenerative capabilities in response to injury. Chronic pancreatitis (CP) is a risk factor for pancreatic cancer. The underlying mechanisms for PDA progression in CP patients are incompletely understood and are likely multifactorial, including both genetic and environmental insults (5). Studies have shown that cytokines and reactive oxygen species generated during chronic inflammation can cause DNA damage. It has been hypothesized that an unlucky pancreatic cell might acquire DNA damage in the protooncogene *KRAS* or tumor suppressor genes *TP53* or *CDKN2A*, thereby accelerating malignant transformation (6, 7). Thus, it is imperative to understand the mechanisms by which DNA damage occurs in the setting of CP. Duct obstruction is one cause of CP, and the ability of ductal cells to acquire DNA damage in the setting of CP is incompletely understood.

In this report, we conducted single-cell RNA sequencing (scRNA-seq) on homeostatic murine pancreatic duct, intrapancreatic bile duct, and pancreatobiliary cells using a DBA^+ lectin sorting strategy, and present a high-resolution atlas of these murine duct cells. By extensively comparing our subpopulations to previously reported mouse and human pancreatic duct subpopulations (8-10), we both corroborate several previous findings and identify and validate novel duct cell heterogeneity with unique functional properties including roles for subpopulation markers in CP. Our findings suggest that multiple duct subpopulations retain progenitor capacity, which is influenced by expression of markers driving subpopulation identity.

RESULTS

scRNA-seq identifies multiple pancreas cell types with DBA lectin sorting

Previously reported subpopulations of murine pancreatic duct cells were identified by single cell analysis of pancreatic cells obtained using an islet isolation procedure; thus, exocrine duct cells were of low abundance (9). To circumvent this issue, we employed a DBA lectin sorting strategy that has been extensively used to isolate and characterize all murine pancreatic duct cell types (11, 12), to investigate murine duct heterogeneity. We isolated live DBA^+ cells from the pancreata of four adult female C57BL/6J littermates, and performed scRNA-seq on the pooled cells using the 10X Genomics platform (Figure 1A and S1A). After filtering out doublets and low-quality cells (defined by low transcript counts), our dataset contained 6813 cells. Clustering analysis identified 16 distinct cell populations with an average of 5345 transcripts per cell and 1908 genes per cell (Figure 1B and Dataset S1). Significantly differentially expressed genes (DEGs) when comparing a cluster to all other clusters are listed in Dataset S2. Annotation of these 16 clusters was accomplished by analysis of known markers (Figure 1B-D). Our dataset comprises 2 populations of ductal cells, a cluster of endothelial cells, one cluster of fibroblasts, and 12 immune cell clusters. As expected, murine endocrine and acinar cells are not present in our dataset because they are not DBA^+ cells. Gene and transcript counts for each cluster are shown in Figure S1B. We identified DBA^+Collagen I^+ fibroblasts and DBA^+CD45^+ immune cells by immufluorescence. $CD31^+$ endothelial cells are not DBA^+. Their presence in our dataset might be explained by the close juxtaposition of pancreatic duct cells with endothelial cells throughout the murine pancreas (Figure S1C).

Subpopulations of ductal cells are characterized by unique gene signatures and regulation of pathways

To get a better understanding of duct cell heterogeneity, we generated an Uniform Manifold Approximation and Projection (UMAP) plot using all duct cells (clusters 0 and 8), which revealed six distinct ductal clusters. Annotation of each duct cluster was accomplished using DEGs, Ingenuity Pathways Analysis (IPA) and upstream regulator analysis, and marker validation in murine and human pancreas (Figure 2A-D, Figure S1D-E, and Datasets S2-S4). Gene and transcript counts for each cluster are shown in Figure S1F and Dataset S1. We observed variable expression of known ductal markers within clusters. Notably, fewer murine duct cells express the transcription factor Hnf1b when compared to Sox9. This observation is in contrast to a previous report demonstrating a similar prevalence of adult murine Hnf1b$^+$ and Sox9$^+$ duct cells, which might be explained by different ductal cell isolation methods (Figure S1G) (13).

Cluster 0

Cluster 0 contains the most cells of all duct clusters in the dataset (Dataset S1). A gene that positively regulates Ras signaling *Mmd2*, the voltage-gated potassium channel protein encoded by *Kcne3*, as well as the ATP-binding cassette (ABC) transporter chloride channel protein encoded by *Cftr,* were significantly upregulated in cluster 0 when compared to all other ductal clusters (Figure 2C and Dataset S2). IPA showed upregulation of hepatic fibrosis signaling pathway in cluster 0 (Figure 2D and Dataset S3). IPA upstream regulator analysis predicted an activated state for the transcriptional regulator *Ctnnb1* in cluster 0. Predicted activation of D-glucose and growth factors Fgf2, Lep, and Hgf, suggest cluster 0 is a metabolically active duct cell subpopulation (Dataset S4). Notably, cluster 0 shows upregulation or activation of multiple genes whose alteration play important roles in the pathophysiology of pancreatic diseases such as *CFTR* for hereditary chronic pancreatitis (14) and *TGFB2* and *CTNNB1* for pancreatic cancer (15-17) (Dataset S2).

To validate gene expression patterns and determine the location of cluster 0 cells within the hierarchical pancreatic ductal tree (18), we next examined expression of select significantly DEGs. *Gmnn*, an inhibitor of DNA replication, was present in both clusters 0 and 2, so we decided to examine histologically, and were surprised to find rare protein expression of *Gmnn*, which was in contrast to the widespread RNA expression depicted by the feature plot (Figure S2A). After examining more than 1500 main pancreatic duct cells from 5 donors, we were unable to find a GEMININ positive cell, indicating very low or absent expression of *GMNN* in human main pancreatic ducts. *Spp1*, which encodes for Osteopontin, and *Wfdc3*, which are significantly DEGs in both clusters 0 and 2, show cytoplasmic expression in all mouse and human pancreatic duct types (Figure S2B-C and Table S1).

Cluster 1

Cells in cluster 1 have significantly upregulated expression of the exosome biogenesis gene *Rab27b* as well as *Ppp1r1b* that encodes for a molecule with kinase and phosphatase inhibition activity (Figure 2A-C and Dataset S2). IPA upstream regulator analysis predicted an activated state for the transcriptional regulator *Smarca4* and the two growth factors Tgfb1 and Gdf2 (Dataset S4). IPA results showed an enrichment in molecules regulating Calcium Transport I (Figure 2D and Dataset S3). Intracellular calcium signaling in pancreatic duct cells is an important regulator of homeostatic bicarbonate secretion (19). *PPP1R1B*, *SMARCA4*, and *TGFB1* have well described roles in the pathogenesis of pancreatic cancer (20-22). We observed expression of markers of cluster 1, *Anxa3* and *Pah*, which are also DEGs in cluster 4, to have cytoplasmic expression in all mouse and human pancreatic duct types (Figure S3A-B and Table S1). Co-

staining of CFTR, a marker of cluster 0, and ANNEXIN A3 show both overlapping and non-overlapping patterns of expression in human intercalated ducts, validating the heterogeneity observed in our murine pancreatic duct dataset in human pancreatic duct cells (Figure S3C).

Cluster 2

Cluster 2 is characterized by low level or lack of expression of multiple ductal cell markers (*Cftr*, *Kcne3*, *Sparc*, *Mmd2, Krt7*) found in other clusters (Figure 2B-C and Figure S1G). IPA analysis showed significant overrepresentation of molecules from several pathways involved in Arginine metabolism in cluster 2 (Figure 2D and Dataset S3). Cluster 2 has the lowest average expression of total genes and transcripts (Figure S1F and Dataset 1). We therefore posit that cluster 2 represents a stable, fairly transcriptionally and metabolically inactive duct cell subpopulation when compared to other duct clusters.

Cluster 3

Cluster 3 cells are located almost entirely within cluster 8 of the UMAP containing 16 DBA^+ clusters (Figure S1E). This, along with high expression of genes regulating cilia biogenesis (*Foxj1*, *Cfap44, Tuba1a*) led to the identification of cluster 3 as intrapancreatic bile duct cells (Figure 2A-C and Dataset S2). Expression of cilia biogenesis genes is more prominent in intrapancreatic bile duct cells when compared to pancreatic duct cells (Figure S3D, Dataset S2, and data not shown). IPA showed upregulation of p53 signaling, NRF2-mediated oxidative stress response, PI3K signaling in B lymphocytes, Senescence pathway among other pathways and inhibition of cell cycle: G1/S checkpoint regulation (Figure 2D and Dataset S3). IPA upstream regulator analysis predicted an activated state for transcriptional regulators *Foxa2*, *Tp53*, *Foxo3*, *Mtpn*, *Tp63*, *Smarca4*, *Nfe2l2*, *Myc*, *Tcf7l2*, *Atf4*, *Pax7*, *Smarcb1*, *Mitf*, *Sp1*, *Rel*, *Lhx1*, *Gli1*, and an inhibited state for transcriptional regulators *Mdm4*, *Gmnn*, and *Hdac1*. Five different microRNAs including mir-17 and mir-25 were all predicted to be in an inhibited state by IPA upstream regulator analysis when compared to all other duct clusters in the dataset (Dataset S4). These results highlight the differences between cellular pathways essential for homeostatic function of pancreatic duct cells and intrapancreatic bile duct cells.

Cluster 4

Cells in cluster 4 have significantly higher expression of *Tgfb3* and *Dclk1* when compared to all other ductal clusters (Figure 2C and Dataset S2). *Dclk1* labels tuft cells which are present in normal murine intrapancreatic bile ducts and pancreatobiliary ductal epithelium, but not in normal murine pancreatic ducts (23). *Dclk1* also marks rare normal murine pancreatic duct cells (24). Clustering analysis of $Dclk1^+$ cells in our dataset showed no subpopulations of $Dclk1^+$ ductal cells (data not shown). IPA showed 144 significantly differentially expressed pathways when comparing cluster 4 to all other ductal clusters (Figure 2D and Dataset S3). Yap, a transcriptional regulator essential for homeostasis of biliary duct cells (25), was predicted to be in an activated state by IPA upstream regulator analysis (Dataset S4). Cluster 4 also contained a small population (13 cells) of *Dmbt1* and *Ly6d*-expressing cells previously identified in extrahepatic biliary epithelium (25) (Figure S4A). These 13 cells appeared as a small population separate from other cells in cluster 4 in the UMAP (Figure 2A). Similar to the IF validation reported for extrahepatic biliary epithelial cells (BECs) (25), our IF validation of *Dmbt1* and *Ly6d*-expressing cells using Cxcl5, another marker of this subpopulation, shows a greater abundance of these cells than what would be expected given the number identified in the clustering analysis (13). It is possible that this cell type is sensitive to single cell dissociation. Cells in cluster 4 are juxtaposed to pancreatic duct cells (clusters 0, 1, and 2) in the UMAP, suggesting transcriptional commonalities with pancreatic duct cells. In addition, *Dmbt1* and *Ly6d*-expressing cells are present in cluster 4, suggesting a bile duct identity. Based on these shared features of bile and pancreas ducts, we postulate that cluster 4 contains pancreatobiliary duct cells.

Cluster 5

Replicating duct cells are characterized by high expression of *Mki67*, *Cenpf*, and *Cenpe* and comprise 1.65% of all duct cells in our dataset (Figure 2A-C, Figure S3D, and Dataset S2). The location of proliferating ductal epithelium is close to clusters containing intrapancreatic bile duct and pancreatobiliary cells. In addition, cluster 5 shares 6/25 DEGs with cluster 3. These data suggest that cluster 5 is comprised primarily of proliferating cluster 3 and 4 cells (Figure 2A, Figure S1E, and Dataset S2). IPA and upstream regulator analysis showed several of the same pathways and factors as those seen in clusters 3 and 4 (Datasets S3-S4). Consistent with previous reports (26, 27), pancreatic duct cells are fairly mitotically inactive.

Summarily, our high resolution single cell analysis has identified the substructure of murine pancreatic duct cells and characterized pancreatobiliary and intrapancreatic bile duct cells.

Comparison of clusters defines heterogeneity within duct subpopulations

We next sought to determine the relationships between duct clusters by examining their similarities and differences. Dendrogram analysis, Pearson's correlation, and DEGs revealed close relationships between clusters 0 and 2 as well as clusters 1 and 4 (Figure 3A-B and Dataset S2). Comparison of clusters 0 and 2 showed only 9 significant DEGs, suggesting a shared core gene expression program (Figure 3C-D). Overrepresentation of molecules regulating the cell cycle was observed in cluster 0 when compared to cluster 2 (Figure 3E). The DEGs upregulated in cluster 0 promote duct cell function (*Cftr*, *Tuba1a*, *Kcne3*), suggesting that cluster 0 comprises workhorse pancreatic duct cells (28).

When comparing pancreatobiliary cells of cluster 4 to pancreatic duct cells in cluster 1, one of the most striking differences is the enrichment in expression of genes regulating assembly of cell junctions including tight junctions, epithelial adherens junction signaling, regulation of actin-based motility by Rho, and actin cytoskeleton signaling. A strong network of stress fibers, comprised of actin filaments, myosin II, and other proteins, that function in bearing tension, supporting cellular structure, and force generation may be important for pancreatobiliary cell function and maintenance (Figure 3F-H and Datasets S3-S4) (29, 30). Cluster 4: *Dmbt1*$^{+}$*Ly6d*$^{+}$ cells are characterized by strong upregulation of pathways regulating Xenobiotic metabolism when compared to all other cluster 4 cells suggesting a prominent role for these cells in the bile acid and xenobiotic system (BAXS) (Figure 3I-K, and Datasets S3-S4) (31). Comparison of intrapancreatic bile duct cells and pancreatobiliary cells showed many unique features of these populations including upregulation of EIF2 signaling in pancreatobiliary cells and upregulation of coronavirus pathogenesis pathway in intrapancreatic bile duct cells (Figure S4B-D and Datasets S3-S4).

Pancreatobiliary cells express a gene signature enriched in several targets of the Hippo signaling pathway Yap

Two subpopulations of adult murine hepatic homeostatic BECs, A and B, have been previously described (25). To determine if these subpopulations are present in intrapancreatic bile duct (cluster 3) and pancreatobiliary cells (cluster 4), we aligned our dataset with an adult hepatic murine BEC scRNA-seq dataset comprised of 2,344 homeostatic BECs (25). Intrapancreatic bile duct and pancreatobiliary cells aligned well with hepatic BECs, with no apparent batch effect (Figure S5A). Intrapancreatic bile duct cells primarily cluster together with hepatic BECs expressing subpopulation B genes, and pancreatobiliary cells primarily cluster together with hepatic BECs expressing subpopulation A genes (Figure S5B-G and Dataset S1-S2). The subpopulation A expression signature contains many genes significantly enriched as Yap targets,

a signature that has been previously proposed to reflect a dynamic BEC state as opposed to defining a unique cell type (25).

DBA$^+$ lectin murine pancreas sorting identifies previously missed ductal subpopulations

To determine the novelty of duct cell heterogeneity manifested using DBA$^+$ lectin sorting of murine pancreas, we next compared our DBA$^+$ murine pancreatic ductal clusters to previously reported subpopulations of mouse and human pancreas duct cells. Using inDrop and an islet isolation pancreas preparation, Baron *et al.* (2016) identified the substructure of mouse and human pancreatic duct cells (9). Two subpopulations of mouse pancreatic duct cells characterized by expression of *Muc1* and *Tff2* (subpopulation 1) and *Cftr* and *Plat* (subpopulation 2) were described. While *Cftr* expression is characteristic of our cluster 0 (Figure 2C), *Muc1*, *Tff2*, and *Plat* expression didn't typify any murine DBA$^+$ pancreatic duct subpopulation (Figure S6A). Two subpopulations were similarly described for human pancreas duct cells characterized by expression of 1) *TFF1*, *TFF2*, *MUC1, MUC20,* and *PLAT* and 2) *CFTR* and *CD44*. *Tff1* is not expressed in murine DBA$^+$ ductal cells (clusters 0-5). *Cd44* is significantly upregulated in pancreatobiliary cells, and *Muc20* as well as *Tff2* are significantly upregulated in 4:*Dmbt1*$^+$*Lyd6*$^+$ cells (Dataset S2 and Figure S6A-B). Dominic Grün *et al*. (2016) previously reported 4 subpopulations of human pancreatic duct cells characterized by expression of *CEACAM6*, *FTH1*, *KRT19*, and *SPP1* using an islet isolation pancreas preparation and the CEL-seq protocol (10). While *Spp1* is significantly upregulated in DBA$^+$ pancreas duct clusters 0 and 2, *Fth1* doesn't characterize any murine DBA$^+$ pancreas duct population, and *Krt19* is significantly upregulated in pancreatobiliary cells (Dataset S2, Figure S1G, and Figure S6C). *CEACAM6* has no mouse homolog. The differences in pancreatic ductal subpopulation identification may be due to single cell methodology (inDrop, CEL-seq, and 10X Genomics), pancreas preparation method (islet isolation vs DBA$^+$ lectin sorting), differences in ductal cell numbers analyzed, or potential differences between mouse and human duct cells.

Six subpopulations of human pancreatic duct cells have been described using the 10X Genomics platform based on sorting for *BMPR1A*/*ALK3* (8). Using AddModuleScore in Seurat, we calculated a score comparing each of our murine duct clusters to the human ALK3$^+$ clusters (Figure S7A-F) (32). Murine pancreatic duct clusters 0-2 had the highest scores when compared to human ALK3$^+$ clusters 1 (*SPP1*$^+$ Stress/harboring progenitor-like cells) and 2 (*TFF1*$^+$ activated/migrating progenitor cells). Murine pancreatobiliary cells (cluster 4) scored the highest when compared to the human ALK3$^+$ cluster 3 (AKAP12$^+$ small ducts). The human ALK3$^+$ cluster 4 (*WSB1*$^+$ centroacinar cells) didn't distinguishably overlap with any DBA$^+$ mouse pancreas ductal clusters. DBA is expressed in murine centroacinar/terminal ducts as early as three weeks of age (33), thus these cells would be expected to be present in our dataset(11). Examination of centroacinar/terminal ductal cell markers *Hes1* (34), *Aldh1a1* (35), and *Aldh1b1* (36) showed broad expression enriched in either clusters 0 and 2 (*Hes1* and *Aldh1b1*) or clusters 1 and 4 (*Aldh1a1*), rather than a distinct subpopulation as is seen in the ALK3$^+$ human pancreatic duct dataset. *Aldh1a7* is negligibly expressed in murine duct clusters 0-5 (Figure S7G). Unlike in mouse DBA$^+$ pancreas ductal clusters, the human ALK3$^+$ dataset contains two ducto-acinar subpopulations characterized by expression of genes enriched in acinar cells. To assess the presence of ducto-acinar cells in adult murine pancreas, we performed immunolabeling for markers of the ALK3$^+$ human ducto-acinar clusters 5 (*CPA1*) and 6 (*AMY2A* and *AMY2B*). Although ducto-acinar cells, like centroacinar/terminal ductal cells, don't define a unique cluster in our DBA$^+$ murine duct subpopulations, we identified DBA$^+$Cpa1$^+$ and DBA$^+$α-amylase$^+$ ducto-acinar cells in adult murine pancreas (Figure S7H). Taken together, these data suggest murine centroacinar/terminal ductal and ducto-acinar cells are largely transcriptionally homogenous with other murine duct cell types.

RaceID3/StemID2 suggest murine DBA$^+$ duct cluster 0 and 2 cells are the most progenitor-like

Given the close relationships observed between DBA$^+$ duct clusters 0 and 2 as well as 1 and 4, we next assessed differentiation potential using RaceID3/StemID2 to predict cell types, lineage trajectories, and stemness (37). Unsupervised clustering with RaceID3 showed 17 clusters. RaceID3 clusters with 10 cells or less were removed from subsequent analyses, and Seurat duct clusters 3 and 5 are not included in this analysis (Figure 4A-B). RaceID3 clusters with the highest StemID2 score correlate to cells present in Seurat duct clusters 0 and 2 (Figure 4C and Figure S8A-B). The variable StemID2 scores observed for cells within Seurat duct clusters 0, 1, 2, and 4 suggest distinct stages of differentiation or maturation. Consistent with previous literature, the pancreatic ductal cell progenitor niche isn't restricted to a single cluster (8).

Pseudotime ordering identifies an epithelial-mesenchymal transition (EMT) axis in pancreatic duct cells

To further examine the lineage relationships among pancreas duct subpopulations, we ordered cells in pseudotime based on their transcriptional similarity (38). Monocle 3 analysis showed DBA$^+$ duct clusters 3 and 5 were disconnected from the main pseudotime trajectory, so we focused our analysis on DBA$^+$ duct clusters 0, 1, 2, and 4 (Figure S8C). Because RaceID3/StemID2 analysis showed Seurat clusters 0 and 2 have the highest StemID scores, we started the pseudotime ordering beginning with cluster 0 as Seurat clusters 0 and 2 are juxtaposed in the Monocle 3 clustering (Figure 4D-E and Figure S8D).

In Monocle 3 analysis, genes with similar patterns of expression that vary over time across the pseudotime trajectory are coalesced into modules (Figure 5A). We performed IPA and upstream regulator analysis, a pairwise comparison, comparing select clusters within a module to analyze the gene expression changes along the pseudotime trajectory (Figure 5B-D and Datasets S3-S5). Examination of pathways deregulated in modules 4 and 14 showed a shift in the molecules driving the Xenobiotic Metabolism CAR Signaling Pathway. The Xenobiotic nuclear receptor CAR is an important sensor of physiologic toxins and plays a role in their removal (39). This pathway is regulated by *Aldh1b1*, *Aldh1l1*, *Gstt2*/*Gstt2b*, *Hs6st2*, and *Ugt2b7* in clusters 0 and 2 and *Aldh1a1*, *Fmo3*, *Gstm1*, and *Sod3* in cluster 1, suggesting that these clusters might respond differently when exposed to toxins or play heterogenous roles in endogenous toxin elimination (Figure 5B-C).

Regulation of the Epithelial Mesenchymal Transition By Growth Factors Pathway was upregulated in cluster 1 when compared to cluster 0 in Module 34. Molecules altered in this pathway play variable roles in promoting the epithelial or mesenchymal state and include *Fgf12*, *Fgfr2*, *Fgfr3*, *Pdgfc*, and *Smad3* (Figure 5D). When comparing clusters 0 and 1, examination of EMT markers *Vim* and *Cdh1* showed a stronger probability of expression of *Cdh1* in cluster 1 and a stronger probability of expression of *Vim* in cluster 0 (Figure 5E). Using immunofluorescence (IF), we detected Vimentin$^+$ ductal cells in both mouse and human pancreas, validating this epithelial-mesenchymal transitional axis (Figure 5F).

SPP1 is required for mature human pancreas duct cell identity

Our analysis thus far has identified and validated multiple transcriptional programs expressed by murine pancreatic duct cells and predicted possible lineage relationships among them. To assess the function of select markers defining murine DBA$^+$ pancreas duct clusters, we next examined the consequences of their loss in the immortalized human duct cell line HPDE E6/E7. *Spp1*, a marker of clusters 0 and 2, has been shown by us and others to mark a pancreas duct cell type enriched in progenitor capacity (8, 40). *Gmnn*, a marker of cluster 0, acts to inhibit re-replication

of DNA during DNA synthesis by inhibiting the prereplication complex (41, 42). *Anxa3*, a marker of clusters 1 and 4, inhibits phospholipase A2 and cleaves inositol 1,2-cyclic phosphate generating inositol 1-phosphate in a calcium dependent manner (43, 44). *PAH* and *WFDC3* were not expressed in HPDE E6/E7 cells (data not shown). We generated and validated *SPP1*, *GMNN*, and *ANXA3* knockout HPDE E6/E7 lines using CRISPR/Cas9 (Figure 6A-C). Strong, consistent phenotypes were observed among different knockout lines for each gene despite some lines not demonstrating full loss of the protein (HPDE E6/E7 *ANXA3* gRNA2 and HPDE E6/E7 *SPP1* gRNAs 1-4). Cellular morphology was similar to the scrambled (scr) gRNA control (45) for every knockout line except HPDE E6/E7 *SPP1* gRNAs 1-4, which displayed a dramatic change in cellular morphology. HPDE E6/E7 *SPP1* knockout cells showed prominent filipodia and significantly increased proliferation in both 2D and 3D assays. HPDE E6/E7 *ANXA3* and *GMNN* knockout lines also show significantly increased proliferative capacity in both 2D and 3D assays, a phenotype suggestive of increased progenitor function (Figure 6D-F, Figure S9A, and data not shown). The change in cellular morphology in HPDE E6/E7 *SPP1* knockout lines is accompanied by decreased duct function as measured by carbonic anhydrase activity (Figure 6G).

To assess the changes in HPDE E6/E7 *SPP1* knockout lines on a molecular scale, we performed bulk RNA-sequencing on all 4 HPDE E6/E7 *SPP1* knockout lines and the HPDE E6/E7 scr gRNA control. A significant increase in markers associated with epithelial-mesenchymal transition (EMT) (*VIM*, *ZEB1*, *TWIST1*, *MMP2*) was observed in HPDE E6/E7 *SPP1* knockout lines when compared to the control (Datasets S2-S4 and Figure 6H-I). Markers of mature duct cells (*HNF1B*, *SOX9*, *KRT19*) were significantly downregulated in HPDE E6/E7 *SPP1* knockout lines when compared to the control (Figure 6H, J-K and Dataset S2). Gene Set Enrichment Analysis (GSEA) showed positive enrichment of pathways that regulate embryogenesis (*HOX* genes and *NOTCH* signaling) and cell cycle regulation in HPDE E6/E7 *SPP1* knockout lines when compared to the HPDE E6/E7 scr gRNA control, supporting the notion that loss of SPP1 leads to a more immature, progenitor-like state (Figure S9B-E). Taken together, these results define unique functional properties for markers that characterize murine DBA^+ pancreas duct cells and suggest that *SPP1* is an essential regulator of human pancreatic duct cell maturation and function.

Geminin safeguards against accumulation of DNA damage in mouse ductal cells in the setting of chronic pancreatitis

One marker of the workhorse population of pancreatic duct cells *Gmnn* has previously been associated with chronic inflammatory diseases such as asthma (46). We therefore queried its role in pancreas inflammatory disease. *Gmnn* binds to Cdt1 and inhibits DNA replication during the S phase. Geminin is a crucial regulator of genomic stability; its inhibition in multiple cancer cell lines leads to DNA re-replication and aneuploidy (47, 48). To determine the requirement for *Gmnn* in normal homeostatic pancreatic ductal cells, we generated a conditional *Gmnn* floxed allele and crossed the mouse to the *Sox9–Cre*^{ERT2} (49) and *Hnf1b–Cre*^{ERT2} (50) lines (Figure S10). Adult mice, between the ages of 7-9 weeks, were injected with tamoxifen to ablate Geminin in mouse pancreatic duct cells. Tamoxifen injected *Sox9cre*$^{Tg/wt}$; *Geminin*$^{f/f}$, *Sox9cre*$^{Tg/wt}$; *Geminin*$^{f/wt}$, and *Hnf1b*$^{Tg/wt}$; *Geminin*$^{f/f}$ mice displayed no histological abnormalities as assessed by hematoxylin and eosin (H&E) staining and no significant alterations in DNA damage as assessed by ATR and γ-H2AX IF up to 6 months post tamoxifen injection (data not shown). We were unsurprised by these findings, given the low proliferation rate of murine pancreatic duct cells suggested by our single cell data. Thus, Geminin may only be required in the context of pathologies characterized by increased proliferation in the pancreas such as pancreatitis or PDA (51).

We examined proliferation in human pancreas duct cells in CP patients (N=5 patients) and found a significant increase in Geminin expression when compared to normal human pancreatic duct cells (N=10 donors) (Figure 7A-B). Pancreatic duct ligation (PDL), an experimental technique that recapitulates features of human gallstone pancreatitis, results in an increase in proliferation

of rat pancreatic duct cells (52, 53). To investigate the role of Geminin in mouse pancreatic duct cells in the setting of CP, we performed PDL on *Sox9cre*$^{Tg/wt}$; *Geminin*$^{f/f}$, *Sox9cre*$^{Tg/wt}$; *Geminin*$^{f/wt}$, *Hnf1b*$^{Tg/wt}$; *Geminin*$^{f/f}$ and littermate control mice (Figure 7C). As in the human setting, we also observed upregulation of Geminin in ductal epithelium in the control PDL mouse group (Figure 7D). Previously reported features of the PDL model were evident in our transgenic mice including replacement of parenchymal cells with adipose tissue, inflammation, and fibrosis (54, 55) (Figure S11A-B). Significant attenuation of Geminin expression was observed in *Sox9cre*$^{Tg/wt}$; *Geminin*$^{f/f}$, *Sox9cre*$^{Tg/wt}$; *Geminin*$^{f/wt}$, and *Hnf1b*$^{Tg/wt}$; *Geminin*$^{f/f}$ mouse pancreatic duct cells when compared to controls (Figure 7D and Figure S12A). Homozygous *Gmnn* loss in Sox9^{+} pancreatic ductal cells promoted an acute increase in proliferation, as assessed by BrdU incorporation, at Day 7 which became insignificant at Day 30 (Figures S12B-E). No changes were observed in apoptosis for any model or time point when compared to controls as assessed by cleaved caspase-3 IF (data not shown). Examination of DNA damage by γ-H2AX IF showed significantly increased γ-H2AX foci in *Sox9cre*$^{Tg/wt}$; *Geminin*$^{f/f}$ mice at Day 7, an observation that was sustained at Day 30 (Figure 7E-H). Assessment of DNA damage in *Sox9cre*$^{Tg/wt}$; *Geminin*$^{f/f}$, *Sox9cre*$^{Tg/wt}$; *Geminin*$^{f/wt}$, and *Hnf1b*$^{Tg/wt}$; *Geminin*$^{f/f}$ mice by ATR IF showed no significant changes (data not shown). The lack of phenotypes observed in the *Hnf1b*$^{Tg/wt}$; *Geminin*$^{f/f}$ model may be due to differences in recombination induced by the *Sox9–Cre*^{ERT2} and *Hnf1b–Cre*^{ERT2} lines, since fewer cells of the pancreatic ductal epithelium express Hnf1b (Figure S1G and Figure 7C). Taken together, these data suggest Geminin is an important regulator of genomic stability in pancreatic ductal cells in the setting of CP.

DISCUSSION

We present a single cell transcriptional blueprint of murine pancreatic duct cells, intrapancreatic bile duct cells, and pancreatobiliary cells. Notably, our single cell analysis showed that endothelial cells, fibroblasts, and immune cells are also obtained using the DBA^{+} lectin sorting strategy(12), and suggests that a subsequent ductal purification step is required to obtain pure pancreatic duct cells using this protocol. A static transcriptional picture in time has highlighted a very dynamic view of pancreas duct cell heterogeneity. Our study provokes reinterpretation of several previously published lineage tracing reports using ductal-specific Cre mouse lines, and will help plan future lineage tracing studies.

Cluster 0 workhorse pancreatic duct cells comprise the largest pancreatic duct subpopulation identified. Although clusters 0 and 2 share many markers, we found compelling differences in metabolic states as manifested in part by an overall lower gene and transcript count for cluster 2. IPA suggested that subpopulations of pancreatic duct cells may use different predominant mechanisms for bicarbonate secretion such as Cftr (56) for cluster 0 and calcium signaling for cluster 1 (57). One notable difference between clusters 0 and 2 vs 1 is the molecules which regulate the Xenobiotic Metabolism CAR signaling pathway. We observed expression of several genes, whose alteration contributes to PDA progression including *Tgfb2* and *Ctnnb1* in cluster 0 and *Ppp1r1b, Smarca4,* and *Tgfb1* in cluster 1. IPA upstream regulator analysis of Monocle 3 Module 14 predicted significant inhibition of *Kras* in cluster 1 when compared to cluster 0. Additionally, IPA upstream regulator analysis comparing cluster 2 vs 0 in Module 19 predicted activation of Myc and Mycn in cluster 2. These genes play central roles in homeostasis of pancreatic duct cells, and it's possible that distinct ductal cell subpopulations which are actively expressing these pathways may have different predispositions to PDA with mutations in these genes, heterogeneity which may also contribute to development of different subtypes of PDA.

We identified an EMT axis in pancreatic duct cells using Monocle 3 and validated this observation in mouse and human duct cells. *Spp1* is one gatekeeper of this epithelial to mesenchymal transitory duct phenotype as manifested by loss of ductal markers, reduced duct function, and upregulation of EMT genes in HPDE E6/E7 *SPP1* knockout cells when compared

to controls. Clusters 0 and 2, characterized by strong expression of *Spp1*, show the highest StemID2 scores. *SPP1* knockout HPDE E6/E7 cells display prominent filipodia and the highest proliferative capacity of all markers examined when compared to controls. Taken together, these phenotypes along with upregulation of pathways regulating mammalian development (Notch signaling and Hox genes) manifested by GSEA suggest SPP1 loss promotes human duct cell de-differentiation.

In human pancreas duct cells, the subpopulation characterized by *SPP1* expression is described as “stress/harboring progenitor-like cells” (8). We observed significant deregulation of 14 cancer-related IPA pathways for which pathway directionality was known in HPDE E6/E7 *SPP1* knockout lines vs HPDE E6/E7 scr gRNA controls. 13/14 of these cancer-related pathways, including Pancreatic Adenocarcinoma Signaling, were in a direction suggestive that *SPP1* loss protects against tumor progression in human pancreatic duct cells. These findings are in agreement with published studies suggesting that *SPP1* loss ameliorates aggressiveness of pancreatic cancer cells (58, 59) and colon cancer cells (60, 61).

The requirement for Geminin in prevention of DNA re-replication initiation has been postulated to be when cells are stressed to divide quickly (62). We were unable to detect DNA damage with Geminin loss in homeostatic pancreatic duct cells, which may be due to the low proliferation rate of pancreatic duct cells and/or the presence of compensatory mechanisms with redundant function, such as ubiquitin-dependent degradation of Cdt1 at the time of replication licensing (63-66). Compensatory mechanisms are not sufficient to rescue the effects of Geminin loss in pancreatic duct cells in the context of CP, the result of which is accumulation of sustained DNA damage evident by γ-H2AX, but not ATR labeling. It has been previously reported that ATR is activated in Geminin-depleted colon cancer cell lines (67). Activation of the ATR-Chk1 pathway isn’t a major player in pancreatic duct cells in the setting of CP (68), suggesting different mechanisms participate in sensing Geminin depletion-induced DNA damage in different experimental systems and tissues.

MATERIALS AND METHODS

Preparation of pancreatic duct cells for single cell analysis

Pancreata from four 9 week old female C57BL/6J littermates (Jackson Labs, Stock 000664) were dissected, digested into single cells, and the DBA^+ fraction obtained as previously described (12). Subsequently, live DBA^+ cells were isolated for scRNA-seq by excluding propidium iodide (Thermo Fisher Scientific, P3566) positive single cells during FACS. scRNA-seq was performed by the Institute for Human Genetics Genomics Core Facility at University of California San Francisco (UCSF) using the 10X Genomics platform. Briefly, live, single, DBA^+ pancreatic cells were loaded onto the microfluidic chip to generate single cell GEMs (Gel Bead-In EMulsions). Following cell lysis and unique barcode labeling, the cDNA library of 18,624 live pancreatic cells was generated using the Chromium Single Cell 3' GEM, Library & Gel Bead Kit v2 (10X Genomics). The cDNA library was sequenced on one lane using an Illumina HiSeq 4000.

Single cell RNA-seq data processing

scRNA-seq data was generated on the 10X platform (10X Genomics, Pleasanton, CA) according to Single Cell 3’ protocol (v2 Chemistry) recommended by the manufacturer (69). The Cell Ranger software pipeline (version 2.1.1) was used to demultiplex cellular barcodes, map reads to the genome and transcriptome using the STAR aligner, and produce a matrix of gene counts versus cells. Doublets were filtered by excluding cells having RNA counts > 30000 and mitochondrial genes percentage > 10% in addition to using Scrublet (70). The R package Seurat (71) was used to process the unique molecular identifier (UMI) count matrix and to perform data normalization (gene expression measurements for each cell were normalized by total expression, and log-transformed), dimensionality reduction, clustering, ductal cell isolation, and differential expression

analysis. We identified three clusters enriched in genes from 2 different cell types including: 1) acinar and T cell, 2) acinar cell and macrophage and 3) acinar cell and duct cell. Because our dataset doesn't contain a population of acinar cells (they aren't DBA^+), doublet detector algorithms won't remove acinar cell doublets from our dataset. Based on this reasoning, we removed these clusters containing a high threshold level of expression of acinar cell genes.

Generation of *Geminin* conditional floxed allele

The general strategy to achieve Cre recombinase-mediated conditional gene ablation was to flank exons 3 and 4 of *Mus musculus Gmnn* by *loxP* sites (Figure S10A). The arms of homology for the targeting construct were amplified from BAC clone RP23-92G13 by PCR with high fidelity Taq polymerase. One primer contained a *loxP* site and a single SphI site which was used to verify the presence of the *loxP* site associated with it. Finally, the selectable cassette *CMV-hygro-TK* was incorporated into the targeting vector. The selectable marker itself was flanked by two additional *loxP* sites generating a targeting vector containing three *loxP* sites. Such a strategy allows the generation of ES cells with both a knockout allele and a conditional knockout allele after Cre mediated removal of the selection cassette *in vitro*. The targeting vector was sequenced to guarantee sequence fidelity of exons 3-4 and the proper unidirectional orientation of the three *loxP* sites. The complete left arm of homology was about 3200bp in length and the right arm of homology was 2100bp in length.

V6.5 ES cells were electroporated (25μF, 400V) with the three *loxP* sites-containing targeting construct, and hygromycin selection was performed to identify correctly targeted ES cells. Successfully targeted ES cells (*3loxP*) were identified with Southern blot (Figure S10B). These *3loxP* ES cells were then electroporated with a Cre-expressing plasmid and counter-selected with ganciclovir. ES cells that contained either one *loxP* or two *loxP* sites, respectively, were identified by Southern blot (Figure S10C). An ES cell clone was chosen that carried the conditional knockout allele (two *loxP* sites flanking exons 3 and 4) and was used for blastocyst injections to generate chimeric founder mice. $Gmnn^{f/f}$ mice displayed normal litter sizes. For routine genotyping of $Gmnn^{f/f}$ mice, the primers GCCTCGAACTCAGAAATCCA (primer A) and AACACAAAATTTGGCCTGCT (primer B) were used. To identify the deleted allele by PCR, primer C (TAGCCCGGACTACACAGAGG) can be used with primer A.

Southern blot

For Southern blotting of genomic DNA, samples were digested with SphI or Bsu36I restriction enzymes for at least 4hrs and separated on an 0.8% agarose gel. The DNA was transferred to a Hybond-XL membrane (GE-Healthcare) in a custom transfer setup. Before assembly, the agarose gel was treated for 15min in depurination solution (21.5ml 37% HCl in 1L H_2O), briefly rinsed in H_2O and then soaked in denaturing solution (20g NaOH pellets, 87.6g NaCl in 1L H_2O) for 30min. After transfer, the DNA was crosslinked to the membrane with UV light. The PCR amplified external Southern blot probes were labeled with ^{32}P using the Prime-It II Random Primer Labeling kit from Stratagene. After hybridization of the probe and washing of the membrane, Kodak MS film was exposed to it and then developed.

Mice

The transgenic mouse strain *Sox9–Cre*^{ERT2} was obtained from Jackson Labs (Stock 018829), and *Hnf1b–Cre*^{ERT2} has been previously described (50). Mice were maintained on a mixed genetic background. To induce Cre recombination, mice were injected with 6.7mg tamoxifen (Actavis, NDC 0591-2473-30) via oral gavage three different days over the course of a week at 7-9 weeks of age. Pancreatic duct ligations were performed as previously described (72). BrdU (Sigma, B9285-1G) injections were performed 24 hours and 4 hours prior to dissection. Mice were genotyped by PCR or Transnetyx. All animal studies were approved by the Institutional Animal Care and Use Committee at UCSF.

Histology/immunostaining

Tissues were fixed in Z-Fix (Anatech Ltd., 174), processed according to a standard protocol, and embedded in Paraplast Plus embedding agent for histology, with DMSO (VWR 15159-464).
For immunostaining, paraffin sections were deparaffinized, rehydrated, and antigen retrieval was performed, for all antibodies except BrdU, with Antigen Retrieval Citra (Biogenex, HK086-9K) using a heat-mediated microwave method. For immunostaining of BrdU, antigen retrieval was performed as previously described (73). For IHC, endogenous peroxidase activity was blocked by incubation with 3% hydrogen peroxide (Fisher Scientific, H325-100) following antigen retrieval. Primary antibodies were incubated overnight at 4°C. Secondary antibodies were used at 1:500 and incubated at room temperature for 1 hour (IHC) or 2 hours (IF). For IF, slides were mounted in ProLong Diamond Antifade Mountant with DAPI (ThermoFisher, P36962). For IHC, Vectastain Elite ABC kit (Vector Laboratories, PK-6100) and DAB Peroxidase (HRP) Substrate kit (Vector Laboratories, SK-4100) were used. Primary antibodies used in this study are listed in Table S2. Secondary antibodies used in this study were obtained from Life Technologies and Jackson Immunoresearch.

Immunostaining of cluster markers as well as the types of ducts within the ductal hierarchy tree were reviewed and classified by a board-certified pathologist. For expression analysis of selected markers in murine and human tissues, images shown are representative of at least 3 different donors or 9 week-old C57BL/6J mice. For quantification of BrdU, cleaved caspase 3, Geminin, Ki67, H2AX, and ATR, at least 60 cells from 3 different ducts were analyzed. Normal human tissue used in this study was obtained from research consented human cadaver donors through UCSF's Islet Production Core. Human pancreatic tissue specimens from five surgical resections from patients without pancreaticobiliary carcinoma or high grade pancreatic intraepithelial neoplasia were obtained. The pancreatic histologic section demonstrated chronic pancreatitis with loss of acinar parenchyma resulting in atrophic lobules along with variable fibrosis and chronic inflammation (most had no to sparse lymphocytic inflammation).

Immunocytochemistry

Cells were grown on coverslips in 6 well plates and fixed at RT for 15 minutes with 4% paraformaldehyde. Cells were permeabilized with permeabilization solution (0.1% w/v Saponin, 5% w/v BSA in PBS-/-). The primary antibody was incubated in permeabilization solution at 4°C overnight. After washing off unbound primary antibody with PBS-/-, the secondary antibody was incubated in permeabilization solution for 1 hour at RT. After washing off unbound secondary antibody with PBS-/-, cells were mounted using ProLong Diamond Antifade Mountant with DAPI (ThermoFisher, P36962).

RNA-seq

RNA was isolated using the RNeasy Mini Kit (Qiagen, 74106) as per manufacturer's instructions. To obtain N=3 for the HPDE E6/E7 scr gRNA control, RNA was isolated on 3 different days of subsequent passages. A stranded mRNA library prep was prepared using PolyA capture and paired-end sequencing was performed by Novogene. 40 million reads were sequenced for each sample. Quality of raw FASTQ sequences was assessed using FASTQC. To process RNA-Seq libraries, adaptor sequences were trimmed using Cutadapt version 1.14 (requiring a length greater than 10 nt after trimming) and quality-filtered by requiring all bases to have a minimum score of 20 (-m 20 -q 20). Only reads that passed the quality or length threshold on both strands were considered for mapping. Reads were aligned to the human genome GRCh38 (hg38) with the STAR Aligner (version 020201). Ensembl reference annotation version 89 was used to define gene models for mapping quantification. Uniquely mapped reads for each gene model were produced using STAR parameter "--quantMode GeneCounts." Differential expression analysis was performed in R using DESeq2 (v.1.16.0) with the default parameters, including the Cook's

distance treatment to remove outliers. The RNA-seq and scRNA-seq datasets were deposited to GEO (GEO accession #GSE159343).

Cell culture assays

HPDE E6/E7 cells (74) were cultured in DMEM (Life Technologies 11995073), 10% FBS (Corning, 35011CV), 1X Penicillin : Streptomycin solution (Corning, 30-002-CI). For CellTiter-Glo Luminescent Cell Viability Assays (Promega, G7570), 1500 cells were seeded in quadruplicate per cell line in a 96 well plate in 150uL media, and luminescence was measured 5 days after plating cells. Values depicted for all cell culture experiments represent the average of at least 3 independent experiments.

For 3D proliferation assays, 1000 cells were seeded in triplicate per cell line in a drop of growth-factor reduced Matrigel (Corning, 356231) diluted 1:1 with complete HPDE media. After 4 days, images were taken of each well. For quantification, at least 40 individual spheroids per well were manually circled and the area determined using ROI tools from ImageJ (version 2.0.0). The average area of each well was normalized to the average from triplicate wells of the HPDE E6/E7 scr gRNA.

For carbonic anhydrase activity assays, cell lysates were prepared using standard protocols and cell lysis buffer (Cell Signaling Technologies, 9803S) containing 100 mM PMSF, 1X cOmplete Protease Inhibitor Cocktail (Roche, 11697498001), and 1X PhosSTOP (Sigma Aldrich, 4906845001). Carbonic anhydrase activity was measured using the Carbonic Anhydrase Activity Assay Kit (Biovision, K472-100). For normalization, equal amounts of protein (10ug) per sample were used in the assay. Protein concentration was determined using the Pierce BCA Protein Assay Kit (Thermo Fisher Scientific, 23225).

Generation of stable knockout HPDE E6/E7 cell lines

For generation of stable knockouts, gRNAs were cloned into eSPCas-LentiCRISPR v2 (Genscript). gRNA sequences are included in Table S3. Each gRNA-containing plasmid was incorporated into lentivirus. HPDE E6/E7 cells were transduced with these lentiviruses, and cells expressing the gRNA-containing plasmid were selected for with puromycin. All cell culture experiments were performed using bulk transduced HPDE E6/E7 cells.

Western blotting

Cell lysates were prepared using standard protocols and RIPA buffer (Thermo Fisher Scientific, 89901) containing 100 mM PMSF, 1X cOmplete Protease Inhibitor Cocktail (Roche, 11697498001), and 1X PhosSTOP (Sigma Aldrich, 4906845001). PVDF membranes were incubated with primary antibodies overnight at 4°C. After RT incubation with the appropriate HRP-conjugated secondary antibody for 1 hour, membranes were developed using SuperSignal West Pico PLUS Chemiluminescent Substrate (Thermo Scientific, 34580).

Bioinformatics and statistical analysis

We used $p \leq 0.05$ as a cutoff for DEG inclusion for IPA and IPA upstream regulator analysis. Due to low cell number and high similarity, some comparisons did not yield an acceptable number of statistically significant DEGs (≤25), and we used a relaxed $p \leq 0.1$ as a cutoff for these in order to identify more targets. GSEA was performed on the identified DEGs with the GSEA software (version 3.0) in the pre-ranked mode, with the Reactome pathway dataset (version 7.2). Data are presented as mean ± SEM and were analyzed in GraphPad Prism or Microsoft Office Excel. Statistical significance was assumed at a *P* value of ≤ 0.05. *P* values were calculated with the unpaired *t*-test. For interpretation of statistical results from unpaired *t*-test, * = *P* value ≤ 0.05, ** = *P* value ≤ 0.01, *** = *P* value ≤ 0.001, and **** = *P* value ≤ 0.0001. For all statistical analyses,

outliers were identified and excluded using the Grubbs' outlier test (alpha = 0.05) or ROUT (Q=10%).

ACKNOWLEDGEMENTS

The authors thank Christina S. Chung, Debbie Ngow, and Melissa Campbell for their indispensable help with mouse colony maintenance, genotyping, and technical assistance. The authors wish to acknowledge Luc Baeyens and Michael S. German for helpful intellectual discussions. Graphical illustrations were developed in part by Jimmy Chen using BioRender.com. The *Gmnn* floxed mouse strain was generated in Rudolf Jaenisch's laboratory. This work was supported by a Richard G. Klein Fellowship in Pancreas Development, Regeneration or Cancer (to A.M.H.). A.M.H. was additionally supported by F32 CA221114 and a Hirshberg Foundation for Pancreatic Cancer Research Seed Grant. A.A.R. and G.K.F. were supported by the UCSF Bakar ImmunoX Initiative. E.A.C. was supported by R01 CA222862. Work in M.H.'s laboratory was supported by R01 CA172045 and a grant from the Parker Institute for Cancer Immunotherapy (PICI). The authors declare no competing interests.

REFERENCES

1. J. M. Bailey *et al.*, p53 mutations cooperate with oncogenic Kras to promote adenocarcinoma from pancreatic ductal cells. *Oncogene* **35**, 4282-4288 (2016).
2. A. Y. L. Lee *et al.*, Cell of origin affects tumour development and phenotype in pancreatic ductal adenocarcinoma. *Gut* **68**, 487-498 (2019).
3. M. Wilschanski, I. Novak, The cystic fibrosis of exocrine pancreas. *Cold Spring Harb Perspect Med* **3**, a009746 (2013).
4. M. V. Apte, J. S. Wilson, M. A. Korsten, Alcohol-related pancreatic damage: mechanisms and treatment. *Alcohol Health Res World* **21**, 13-20 (1997).
5. B. Etemad, D. C. Whitcomb, Chronic pancreatitis: diagnosis, classification, and new genetic developments. *Gastroenterology* **120**, 682-707 (2001).
6. D. Whitcomb, J. Greer, Germ-line mutations, pancreatic inflammation, and pancreatic cancer. *Clin Gastroenterol Hepatol* **7**, S29-34 (2009).
7. P. Dhar, S. Kalghatgi, V. Saraf, Pancreatic cancer in chronic pancreatitis. *Indian J Surg Oncol* **6**, 57-62 (2015).
8. M. M. F. Qadir *et al.*, Single-cell resolution analysis of the human pancreatic ductal progenitor cell niche. *Proc Natl Acad Sci U S A* **117**, 10876-10887 (2020).
9. M. Baron *et al.*, A Single-Cell Transcriptomic Map of the Human and Mouse Pancreas Reveals Inter- and Intra-cell Population Structure. *Cell Syst* **3**, 346-360 e344 (2016).
10. D. Grun *et al.*, De Novo Prediction of Stem Cell Identity using Single-Cell Transcriptome Data. *Cell Stem Cell* **19**, 266-277 (2016).
11. R. L. Beer, M. J. Parsons, M. Rovira, Centroacinar cells: At the center of pancreas regeneration. *Dev Biol* **413**, 8-15 (2016).
12. M. Reichert *et al.*, Isolation, culture and genetic manipulation of mouse pancreatic ductal cells. *Nat Protoc* **8**, 1354-1365 (2013).
13. H. Rezanejad *et al.*, Heterogeneity of SOX9 and HNF1beta in Pancreatic Ducts Is Dynamic. *Stem Cell Reports* **10**, 725-738 (2018).
14. K. L. Raphael, F. F. Willingham, Hereditary pancreatitis: current perspectives. *Clin Exp Gastroenterol* **9**, 197-207 (2016).
15. W. Shen *et al.*, TGF-beta in pancreatic cancer initiation and progression: two sides of the same coin. *Cell Biosci* **7**, 39 (2017).

16. K. J. Gordon, M. Dong, E. M. Chislock, T. A. Fields, G. C. Blobe, Loss of type III transforming growth factor beta receptor expression increases motility and invasiveness associated with epithelial to mesenchymal transition during pancreatic cancer progression. *Carcinogenesis* **29**, 252-262 (2008).
17. P. W. Heiser *et al.*, Stabilization of beta-catenin induces pancreas tumor formation. *Gastroenterology* **135**, 1288-1300 (2008).
18. M. Reichert, A. K. Rustgi, Pancreatic ductal cells in development, regeneration, and neoplasia. *J Clin Invest* **121**, 4572-4578 (2011).
19. J. Maleth, P. Hegyi, Calcium signaling in pancreatic ductal epithelial cells: an old friend and a nasty enemy. *Cell Calcium* **55**, 337-345 (2014).
20. N. Roy *et al.*, Brg1 promotes both tumor-suppressive and oncogenic activities at distinct stages of pancreatic cancer formation. *Genes Dev* **29**, 658-671 (2015).
21. C. J. David *et al.*, TGF-beta Tumor Suppression through a Lethal EMT. *Cell* **164**, 1015-1030 (2016).
22. A. Tiwari *et al.*, Loss of HIF1A From Pancreatic Cancer Cells Increases Expression of PPP1R1B and Degradation of p53 to Promote Invasion and Metastasis. *Gastroenterology* 10.1053/j.gastro.2020.07.046 (2020).
23. K. E. Delgiorno *et al.*, Identification and manipulation of biliary metaplasia in pancreatic tumors. *Gastroenterology* **146**, 233-244 e235 (2014).
24. C. B. Westphalen *et al.*, Dclk1 Defines Quiescent Pancreatic Progenitors that Promote Injury-Induced Regeneration and Tumorigenesis. *Cell Stem Cell* **18**, 441-455 (2016).
25. B. J. Pepe-Mooney *et al.*, Single-Cell Analysis of the Liver Epithelium Reveals Dynamic Heterogeneity and an Essential Role for YAP in Homeostasis and Regeneration. *Cell Stem Cell* **25**, 23-38 e28 (2019).
26. A. S. Moin, P. C. Butler, A. E. Butler, Increased Proliferation of the Pancreatic Duct Gland Compartment in Type 1 Diabetes. *J Clin Endocrinol Metab* **102**, 200-209 (2017).
27. A. E. Butler *et al.*, Pancreatic duct replication is increased with obesity and type 2 diabetes in humans. *Diabetologia* **53**, 21-26 (2010).
28. M. Hayashi, I. Novak, Molecular basis of potassium channels in pancreatic duct epithelial cells. *Channels (Austin)* **7**, 432-441 (2013).
29. K. Burridge, E. S. Wittchen, The tension mounts: stress fibers as force-generating mechanotransducers. *J Cell Biol* **200**, 9-19 (2013).
30. S. Tojkander, G. Gateva, P. Lappalainen, Actin stress fibers--assembly, dynamics and biological roles. *J Cell Sci* **125**, 1855-1864 (2012).
31. W. Dubitzky, O. Wolkenhauer, K. H. Cho, H. Yokota, *Encyclopedia of systems biology* (Springer Reference, New York, 2013), pp. 4 volumes (xlvii, 2366 pages).
32. H. Alshetaiwi *et al.*, Defining the emergence of myeloid-derived suppressor cells in breast cancer using single-cell transcriptomics. *Sci Immunol* **5** (2020).
33. B. Z. Stanger *et al.*, Pten constrains centroacinar cell expansion and malignant transformation in the pancreas. *Cancer Cell* **8**, 185-195 (2005).
34. D. Kopinke *et al.*, Lineage tracing reveals the dynamic contribution of Hes1+ cells to the developing and adult pancreas. *Development* **138**, 431-441 (2011).
35. M. Rovira *et al.*, Isolation and characterization of centroacinar/terminal ductal progenitor cells in adult mouse pancreas. *Proc Natl Acad Sci U S A* **107**, 75-80 (2010).
36. E. Mameishvili *et al.*, Aldh1b1 expression defines progenitor cells in the adult pancreas and is required for Kras-induced pancreatic cancer. *Proc Natl Acad Sci U S A* **116**, 20679-20688 (2019).
37. J. S. Herman, Sagar, D. Grun, FateID infers cell fate bias in multipotent progenitors from single-cell RNA-seq data. *Nat Methods* **15**, 379-386 (2018).

38. J. Cao *et al.*, The single-cell transcriptional landscape of mammalian organogenesis. *Nature* **566**, 496-502 (2019).
39. Y. E. Timsit, M. Negishi, CAR and PXR: the xenobiotic-sensing receptors. *Steroids* **72**, 231-246 (2007).
40. G. Kilic, J. Wang, B. Sosa-Pineda, Osteopontin is a novel marker of pancreatic ductal tissues and of undifferentiated pancreatic precursors in mice. *Dev Dyn* **235**, 1659-1667 (2006).
41. T. J. McGarry, M. W. Kirschner, Geminin, an inhibitor of DNA replication, is degraded during mitosis. *Cell* **93**, 1043-1053 (1998).
42. A. Ballabeni, R. Zamponi, J. K. Moore, K. Helin, M. W. Kirschner, Geminin deploys multiple mechanisms to regulate Cdt1 before cell division thus ensuring the proper execution of DNA replication. *Proc Natl Acad Sci U S A* **110**, E2848-2853 (2013).
43. J. F. Tait, C. Smith, L. Xu, B. T. Cookson, Structure and polymorphisms of the human annexin III (ANX3) gene. *Genomics* **18**, 79-86 (1993).
44. V. Gerke, S. E. Moss, Annexins: from structure to function. *Physiol Rev* **82**, 331-371 (2002).
45. K. Suzuki *et al.*, In vivo genome editing via CRISPR/Cas9 mediated homology-independent targeted integration. *Nature* **540**, 144-149 (2016).
46. N. Garbacki *et al.*, MicroRNAs profiling in murine models of acute and chronic asthma: a relationship with mRNAs targets. *PLoS One* **6**, e16509 (2011).
47. W. Zhu, M. L. Depamphilis, Selective killing of cancer cells by suppression of geminin activity. *Cancer Res* **69**, 4870-4877 (2009).
48. S. Saxena, A. Dutta, Geminin-Cdt1 balance is critical for genetic stability. *Mutat Res* **569**, 111-121 (2005).
49. J. L. Kopp *et al.*, Sox9+ ductal cells are multipotent progenitors throughout development but do not produce new endocrine cells in the normal or injured adult pancreas. *Development* **138**, 653-665 (2011).
50. M. Solar *et al.*, Pancreatic exocrine duct cells give rise to insulin-producing beta cells during embryogenesis but not after birth. *Dev Cell* **17**, 849-860 (2009).
51. M. R. Salabat *et al.*, Geminin is overexpressed in human pancreatic cancer and downregulated by the bioflavanoid apigenin in pancreatic cancer cell lines. *Mol Carcinog* **47**, 835-844 (2008).
52. S. Githens, The pancreatic duct cell: proliferative capabilities, specific characteristics, metaplasia, isolation, and culture. *J Pediatr Gastroenterol Nutr* **7**, 486-506 (1988).
53. N. I. Walker, A. W. Pound, An autoradiographic study of the cell proliferation during involution of the rat pancreas. *J Pathol* **139**, 407-418 (1983).
54. A. A. Aghdassi *et al.*, Animal models for investigating chronic pancreatitis. *Fibrogenesis Tissue Repair* **4**, 26 (2011).
55. C. Rastellini *et al.*, Induction of chronic pancreatitis by pancreatic duct ligation activates BMP2, apelin, and PTHrP expression in mice. *Am J Physiol Gastrointest Liver Physiol* **309**, G554-565 (2015).
56. H. Ishiguro *et al.*, CFTR functions as a bicarbonate channel in pancreatic duct cells. *J Gen Physiol* **133**, 315-326 (2009).
57. H. Ishiguro *et al.*, Physiology and pathophysiology of bicarbonate secretion by pancreatic duct epithelium. *Nagoya J Med Sci* **74**, 1-18 (2012).
58. A. Kolb *et al.*, Osteopontin influences the invasiveness of pancreatic cancer cells and is increased in neoplastic and inflammatory conditions. *Cancer Biol Ther* **4**, 740-746 (2005).
59. C. R. Adams *et al.*, Transcriptional control of subtype switching ensures adaptation and growth of pancreatic cancer. *Elife* **8** (2019).
60. R. Ishigamori *et al.*, Osteopontin Deficiency Suppresses Intestinal Tumor Development in Apc-Deficient Min Mice. *Int J Mol Sci* **18** (2017).

61. H. Zhao *et al.*, The role of osteopontin in the progression of solid organ tumour. *Cell Death Dis* **9**, 356 (2018).
62. K. A. Barry, K. M. Schultz, C. J. Payne, T. J. McGarry, Geminin is required for mitotic proliferation of spermatogonia. *Dev Biol* **371**, 35-46 (2012).
63. E. E. Arias, J. C. Walter, Replication-dependent destruction of Cdt1 limits DNA replication to a single round per cell cycle in Xenopus egg extracts. *Genes Dev* **19**, 114-126 (2005).
64. S. L. Kerns, S. J. Torke, J. M. Benjamin, T. J. McGarry, Geminin prevents rereplication during xenopus development. *J Biol Chem* **282**, 5514-5521 (2007).
65. A. Li, J. J. Blow, Cdt1 downregulation by proteolysis and geminin inhibition prevents DNA re-replication in Xenopus. *EMBO J* **24**, 395-404 (2005).
66. D. Maiorano, L. Krasinska, M. Lutzmann, M. Mechali, Recombinant Cdt1 induces rereplication of G2 nuclei in Xenopus egg extracts. *Curr Biol* **15**, 146-153 (2005).
67. J. J. Lin, A. Dutta, ATR pathway is the primary pathway for activating G2/M checkpoint induction after re-replication. *J Biol Chem* **282**, 30357-30362 (2007).
68. J. Smith, L. M. Tho, N. Xu, D. A. Gillespie, The ATM-Chk2 and ATR-Chk1 pathways in DNA damage signaling and cancer. *Adv Cancer Res* **108**, 73-112 (2010).
69. G. X. Zheng *et al.*, Massively parallel digital transcriptional profiling of single cells. *Nat Commun* **8**, 14049 (2017).
70. S. L. Wolock, R. Lopez, A. M. Klein, Scrublet: Computational Identification of Cell Doublets in Single-Cell Transcriptomic Data. *Cell Syst* **8**, 281-291 e289 (2019).
71. R. Satija, J. A. Farrell, D. Gennert, A. F. Schier, A. Regev, Spatial reconstruction of single-cell gene expression data. *Nat Biotechnol* **33**, 495-502 (2015).
72. S. De Groef *et al.*, Surgical Injury to the Mouse Pancreas through Ligation of the Pancreatic Duct as a Model for Endocrine and Exocrine Reprogramming and Proliferation. *J Vis Exp* 10.3791/52765, e52765 (2015).
73. S. Puri *et al.*, Replication confers beta cell immaturity. *Nat Commun* **9**, 485 (2018).
74. T. Furukawa *et al.*, Long-term culture and immortalization of epithelial cells from normal adult human pancreatic ducts transfected by the E6E7 gene of human papilloma virus 16. *Am J Pathol* **148**, 1763-1770 (1996).

Main figure captions

Figure 1. Transcriptomic map of DBA$^+$ pancreatic cells. A) Schematic of experiment workflow. B) The UMAP depicts murine pancreatic DBA$^+$ cells obtained using the protocol. C) A matrix plot shows average expression of ductal cell markers in all clusters, identifying clusters 0 and 8 as ductal cells. D) Feature plots illustrate markers of various cell types including epithelial (*Epcam*), ductal (*Krt19* and *Sox9*), CD45$^+$ immune cells (*Ptprc*), endothelial cells (*Pecam1*), fibroblasts (*Col1a1*), endocrine cells (*Chga*), and acinar cells (*Pnliprp1*). We observed low level expression of acinar cell markers uniformly across all clusters that is likely contaminating acinar cell mRNA.

Figure 2. Transcriptomic map of DBA$^+$ pancreatic duct cells. A) UMAP depicts identity of clusters. B) The dot plot shows the top five significantly DEGs with the highest fold change for each cluster. C) Feature plots show expression of significantly DEGs for clusters 0, 1, 3, 4, and 5. Cluster 2 is characterized by lack of or low level expression of significantly DEGs found in other clusters. D) IPA results show the top 8 deregulated pathways when comparing a cluster to all other clusters. The ratio line indicates the fraction of molecules significantly altered out of all molecules that map to the canonical pathway from within the IPA database. A positive z-score represents upregulation, and a negative z-score indicates downregulation of a pathway in that cluster when compared to all other clusters. A gray bar depicts significant overrepresentation of a pathway, the direction of which cannot yet be determined.

Figure 3. Comparison of ductal clusters 0 vs 2, 4 vs 1, and 4 vs 4:*Dmbt1$^+$Ly6d$^+$*. A) The cluster dendrogram created using dims (used to define the cluster) shows the Euclidean relationships between clusters. The tree is calculated in the PCA space. The genes used to define the tree were set as the variable features of the object. B) Pearson's correlation calculated using average gene expression is depicted. C) Stacked violin plots show five DEGs sharing similar expression patterns in clusters 0 and 2. D) The dot plot shows all 9 DEGs found when comparing clusters 0 vs 2. E) The top 8 altered pathways from IPA comparing clusters 0 vs 2 are depicted. F) Stacked violin plots show five DEGs sharing similar expression patterns in clusters 4 and 1. G) The dot plot shows the top 20 DEGs ranked by fold change when comparing clusters 4 vs 1. H) The top 8 deregulated pathways from IPA comparing clusters 4 vs 1 are depicted. I) Stacked violin plots of five DEGs sharing similar expression patterns in clusters 4:*Dmbt1$^+$Ly6d$^+$* and 4. J) The dot plot shows the top 20 DEGs ranked by fold change when comparing clusters 4:*Dmbt1$^+$Ly6d$^+$* and 4. K) The top 8 changed pathways from IPA comparing clusters 4:*Dmbt1$^+$Ly6d$^+$* and 4 are depicted.

Figure 4. RaceID3/StemID2 predict clusters 0 and 2 have the highest progenitor potential. A) The lineage tree inferred by StemID2 is shown in the RaceID3 clusters. Node color represents the level of transcriptome entropy, edge color describes level of significance, and edge width describes link score. B) Heat map depicts expression of top 5 DEGs in RaceID3 clusters with FDR < 0.01 and fc > 1.2. C) StemID2 scores for RaceID3 clusters are graphed. D) Monocle 3 clustering of murine DBA$^+$ duct clusters 0, 1, 2, and 4 are depicted. E) Each cell's relative pseudotime value is depicted that is a measurement of the distance between its position along the trajectory and the starting point (cluster 0).

Figure 5. Monocle 3 analysis reveals an epithelial mesenchymal axis in pancreatic duct cells. A) Expression changes of the modules generated by Monocle 3 analysis are shown for each cluster. B-D) Expression of modules 4, 14, and 34 along with select IPA results of the top 10 deregulated pathways are shown. Genes in parenthesis are altered in the pathway containing an asterisk in the bar. E) Stacked violin plots show expression of genes in the Regulation of the

Epithelial Mesenchymal Transition By Growth Factors Pathway in DBA^+ duct clusters 0-5. F) IF depicts $CK19^+$ $Vimentin^+$ copositive pancreatic duct cells in mouse (yellow arrow) and human. The main pancreatic duct is shown for humans. Scale bars are 50uM.

Figure 6. A-C) Western blot and quantification of western blot images shows expression of ANNEXIN A3, OSTEOPONTIN, and GEMININ in knockout HPDE E6/E7 lines and the control. D) Brightfield images show changes in cellular morphology of HPDE E6/E7 *SPP1* knockout lines. Scale bars are 100 µm. E) Proliferation was assessed in 2D by CTG assays. F) Proliferation was assessed in 3D by seeding 1000 cells in a drop of matrigel. G) Significantly decreased carbonic anhydrase activity is observed in HPDE E6/E7 *SPP1* knockout lines when compared to the control. H) Relative fold changes calculated using RPM values of mesenchymal and duct markers are shown. Average RPM values for *SPP1* are 79.8 ± 43.2 (scr) and 2.8 ± 0.4 (KO), *HNF1B* are 418.5 ± 33.4 (scr) and 1 ± 0.3 (KO), *SOX9* are 1,555.2 ± 124.8 (scr) and 316 ± 38.7 (KO), *KRT19* are 16,789.5 ± 2,431.2 (scr) and 61 ± 60.5 (KO), *CLDN7* are 8,651.8 ± 923.2 (scr) and 112.8 ± 27.7 (KO), *CDH1* are 8,651.8 ± 923.2 (scr) and 112.8 ± 27.8 (KO), and *VIM* are 80.2 ± 29.1 (scr) and 6,879.8 ± 652.6 (KO). I) The top 14 deregulated pathways from IPA are shown comparing HPDE E6/E7 *SPP1* KO vs HPDE E6/E7 scr gRNA control. J) Immunocytochemistry (ICC) demonstrated reduced Osteopontin expression in HPDE E6/E7 *SPP1* gRNA2 and HPDE E6/E7 *SPP1* gRNA4 when compared to HPDE E6/E7 scr gRNA. Vimentin ICC depicts organized intermediate filaments in HPDE E6/E7 *SPP1* gRNA2 and HPDE E6/E7 *SPP1* gRNA4 while HPDE E6/E7 scr gRNA cells show diffuse, light labeling. Scale bar is 50 µm. K) CK19 ICC shows organized intermediate filaments in HPDE E6/E7 scr gRNA cells while HPDE E6/E7 *SPP1* gRNA2 and HPDE E6/E7 *SPP1* gRNA4 cells display punctate CK19 labeling, where present. Scale bar denotes 50 µm.

Figure 7. *Gmnn* is a regulator of genomic stability in mouse pancreatic duct cells during chronic pancreatitis. A-B) IF images and quantification show a significant increase in proliferation in pancreatic duct cells in CP patients when compared to normal human pancreatic duct cells. C) A schematic of tamoxifen and BrdU administration is shown. The UMAP depicts the pancreatic cells (clusters 0-2) that were analyzed in this experiment. The Venn diagram shows the number of cells in clusters 0-2 that are $Sox9^+$, $Hnf1b^+$, and $Sox9^+Hnf1b^+$ copositive. D) Quantification of Geminin positive ductal cells at Day 7 in *Sox9cre*$^{Tg/wt}$; *Geminin*$^{f/f}$, *Sox9cre*$^{Tg/wt}$; *Geminin*$^{f/wt}$, *Hnf1b*$^{Tg/wt}$; *Geminin*$^{f/f}$ and control mice is depicted. E-F) Representative IF images and quantification of γ-H2AX positive foci is shown at Day 7 in the PDL transgenic models. G-H) Representative IF images and quantification of γ-H2AX positive foci are shown at Day 30 in the *Sox9cre*$^{Tg/wt}$; *Geminin*$^{f/f}$ and control PDL models. All scale bars in this figure are 50 µm.

Supplemental figure captions

Figure S1. Features of DBA^+ (clusters 0-15) and ductal (clusters 0-5) cells. A) The sorting strategy for live, DBA^+ pancreatic cells is displayed. The graph on the left shows the cells plotted by forward and side scatter. In this graph, red cells are PI^+, purple cells are DBA^+PI^-, and blue and green cells are doublets. The graph on the right shows the gating strategy used to sort DBA^+PI^- pancreatic cells. B) The number of genes and transcripts for each cell in clusters 0-15 are shown. C) Co-immunofluorescence labeling identifies $CK19^+DBA^+$ and Collagen I^+DBA^+ copositive pancreatic cells and $CD45^+DBA^+$ copositive pancreatic lymph node cells. Pancreatic $CD31^+$ cells are not DBA^+. A yellow arrow points to a copositive cell. Scale bars are 50 µm. D) The plot shows whether a ductal cell is in cluster 0 or 8 (from the 0-15 cluster dataset) in the 0-5 cluster UMAP. E) This plot depicts the location of the ductal clusters 0-5 in the 0-15 cluster UMAP. F) Violin plots show the number of genes and transcripts in each cell for ductal clusters 0-5. G) Feature plots depict expression of genes normally enriched in pancreatic duct cells.

Figure S2. IHC illustrates expression of markers in clusters 0 and 2 in the mouse and human ductal tree. A) Geminin is expressed in rare ductal cells and acinar cells in the mouse and human pancreas. Yellow arrows point to Geminin positive cells. B) Osteopontin expression is observed in all duct cell types throughout the mouse and human ductal tree as well as in acinar cells. C) Wfdc3 is expressed in all duct cell types in the mouse and human pancreas and in acinar cells. Red arrows point to the indicated duct type. Scale bars are 40 μm.

Figure S3. IHC and IF depict expression of markers in clusters 1, 3, 4, and 5 in mouse and human pancreas duct cells. A) Annexin A3 expression is observed in all ductal cell types in the mouse and human pancreas. The left mouse IHC image under Large duct – Interlobular/Main duct shows Annexin A3 cytoplasmic expression in pancreatobiliary cells and cells within the Ampulla of Vater. Scale bars are 40 μm. B) Pah is expressed in all duct types throughout the mouse and human ductal tree as well as in acinar cells. Scale bars are 40 μm. C) Yellow arrows point to heterogeneous expression of ductal markers Cftr, Annexin A3, and CK19 in human pancreatic duct cells. Scale bars are 20 μm. D) Proliferating and acetylated alpha tubulin positive duct cells are observed in the intrapancreatic bile duct, peribiliary glands, and pancreatobiliary cells in mouse and human. Scale bars are 50 μm.

Figure S4. Characteristics of intrapancreatic bile duct and pancreatobiliary cells. A) Cxcl5, another marker of *Dmbt1*$^{+}$*Ly6d*$^{+}$ cells, positive cells are located in murine and human intrapancreatic bile duct cells, peribiliary glands, and pancreatobiliary cells. Yellow arrows point to ductal cells displaying upregulated Cxcl5. Scale bars are 50 μm. B) Stacked violin plots show expression of 5 genes which are upregulated in clusters 3 and 4. C) The dot plot shows the top 20 DEGs ranked by fold change when comparing clusters 3 vs 4.

Figure S5. Alignment to an adult murine hepatic biliary epithelial cell dataset. A) UMAP showing alignment of adult murine hepatic BECs (blue) to our murine intrapancreatic bile duct cells (red) and pancreatobiliary cells (green). B) Clustering of merged datasets defines 5 clusters. C) Intrapancreatic bile duct cells in DBA^{+} duct cluster 3 are primarily located within the merged clusters 0 and 1, and pancreatobiliary cells in DBA^{+} duct cluster 4 are primarily located within the merged clusters 1 and 2. The heatmap shows the percent of cells from our clusters 3 and 4 within each of the merged clusters 0-4. D) Feature plots depict the 75th percentile and higher of cells expressing the published gene signatures of hepatic BEC subpopulation A and B respectively. E) Cells in clusters 1, 2, and 4 have the strongest enrichment for subpopulation A genes, while cells in clusters 0, 1, and 3 have the strongest enrichment for subpopulation B genes in the merged dataset. F) Dual violin plots show expression of the ductal marker *Sox9* and the Yap targets *Cyr61*, *Ankrd1*, and *Gadd45b* in the merged clusters. G) Dot plot shows expression of hepatic BEC subpopulation A and B genes, analyzed by t-SNE, in Figure 1D of Pepe-Mooney *et al.* (2019) in our murine pancreas DBA^{+} duct clusters 0-5.

Figure S6. Comparison of DBA^{+} lectin sorted mouse pancreas duct cells to previously reported mouse and human duct subpopulations. A-B) Feature plots of genes that characterize subpopulations of mouse and human duct cells in Baron *et al.* (2016). C) Feature plot showing *Fth1* expression, which typifies a human pancreas duct subpopulation in Grün *et al*. (2016).

Figure S7. Comparison of DBA^{+} lectin sorted mouse pancreas duct subpopulations to ALK3^{+} human pancreas duct subpopulations. A-E) Aggregated expression of control feature sets shown in panel A were subtracted from the average expression levels of DEGs for each cluster 0-5 on a single cell level to determine the AddModuleScore comparing each DBA^{+}

pancreas ductal cluster to ALK3$^+$ human pancreas clusters. Panel D shows the number of DEGs in murine DBA$^+$ pancreas duct clusters 0-5 that have a human homolog and could be used in this comparison. F) *Bmpr1a* is expressed in a subset of murine DBA$^+$ pancreas duct cells. G) Stacked violin plots depict expression of centroacinar/terminal ductal cell markers *Hes1*, *Aldh1b1*, *Aldh1a1*, and *Aldh1a7* in DBA$^+$ pancreas duct clusters 0-5. H) Immunostaining identifies ducto-acinar cells in murine pancreas. Yellow arrows point to Cpa1 or α-amylase positive murine ductal cells. Similar to other murine ductal cell markers (Figure S1G), DBA lectin also shows heterogenous expression in murine pancreatic duct cells. Blue arrows point to a DBA lectin negative duct cell. The scale bar is 50um.

Figure S8. RaceID3 clusters and Monocle 3 analysis. A) The location of DBA$^+$ duct cluster 0, 1, 2, and 4 cells in RaceID3 clusters are depicted in Seurat space. Clusters 3 and 5 were not included in this analysis and all clusters with <10 cells were also removed. All removed cells are depicted in the N/A square. B) RaceID3 cluster 10 cells, which have the highest StemID2 score, are depicted in the Monocle 3 UMAP. C) The Monocle 3 UMAP and trajectory are shown when DBA$^+$ duct clusters 0-5 are all included in the analysis. D) A violin plot showing the distribution of cells along the relative pseudotime axis, split by DBA$^+$ duct clusters, is shown. Cluster 4 appears to be the most differentiated from the inferred root, cluster 0.

Figure S9. Characterization of DBA$^+$ murine ductal markers. A) Representative images for 3D proliferation assays are shown. Scale bars are 100 μm. B-E) GSEA enrichments plots for select pathways are depicted.

Figure S10. Generation of 2loxP and 1loxP heterozygous ES cells for mouse *Geminin*. A) The targeting strategy to generate a conditional KO allele for *Geminin* in ES cells is shown. The exact distance between individual exons and their relative sizes is not shown. ES cells heterozygous for the 3loxP allele were obtained through homologous recombination. A Cre recombinase was used to generate ES cells harboring either the 2loxP allele or the 1loxP allele *in vitro.* A SphI restriction site was introduced with the leftmost *loxP* site to allow screening for its presence by Southern blot analysis. B) The 5' probe was used in conjunction with a SphI digest. Besides the wild-type allele, a fragment of about 2.5kb is expected for the 3loxP allele as indicated. Clone 17 and clone H18 tested positive. C) Clone H18 was chosen for Cre treatment *in vitro*. Using a Bsu36I digest and the 5' probe, the 2loxP allele displays a single fragment of the same size as the wild-type allele whereas the 1loxP allele produces a smaller fragment. Bsu36I restriction sites are omitted in the schematic shown in A) for clarity. The 3' probe clearly distinguishes between wild-type, 1loxP, 2loxP, and 3loxP alleles with a SphI digest. Clone 53 was identified as an ES cell clone heterozygous for the conditional 2loxP allele and used for blastocyst injection.

Figure S11. Histology of transgenic PDL models. A-B) Representative H&E images of PDL transgenic models at Day 7 and Day 30 are shown. Scale bars are 40 μm.

Figure S12. Geminin loss causes a transient proliferation response in *Sox9cre*$^{Tg/wt}$; *Geminin*$^{f/f}$ mice. A) Representative IF images of the quantification shown in Figure 7D are depicted. Scale bar is 20 μm. B-C) IF images and quantification of BrdU positive pancreatic ductal cells is shown at Day 7 in the PDL transgenic models. Scale bars are 50 μm. D-E) IF images and quantification of BrdU positive pancreatic ductal cells is shown at Day 30 in the *Sox9cre*$^{Tg/wt}$; *Geminin*$^{f/f}$ and control PDL models. Scale bars are 50 μm.

Table S1. Expression scoring of markers of subpopulations of pancreatic duct cells. This table depicts a summary of expression scoring of selected markers for subpopulations of

pancreatic duct cells in mouse and human tissue. Homogeneous refers to an observed uniform expression level and pattern within a particular ductal cell type. Heterogeneous means that either the observed expression level or pattern varies among cells within a particular ductal cell type.

Table S2. The list of antibodies used in this study.

Table S3. The list of gRNA sequences used in this study.

Dataset S1. Number of cells and average number of genes and transcripts in all Seurat clustering analyses.

Dataset S2. DEGs in various comparisons.

Dataset S3. IPA results.

Dataset S4. IPA Upstream Regulator analysis results.

Dataset S5. Monocle 3 module analysis.

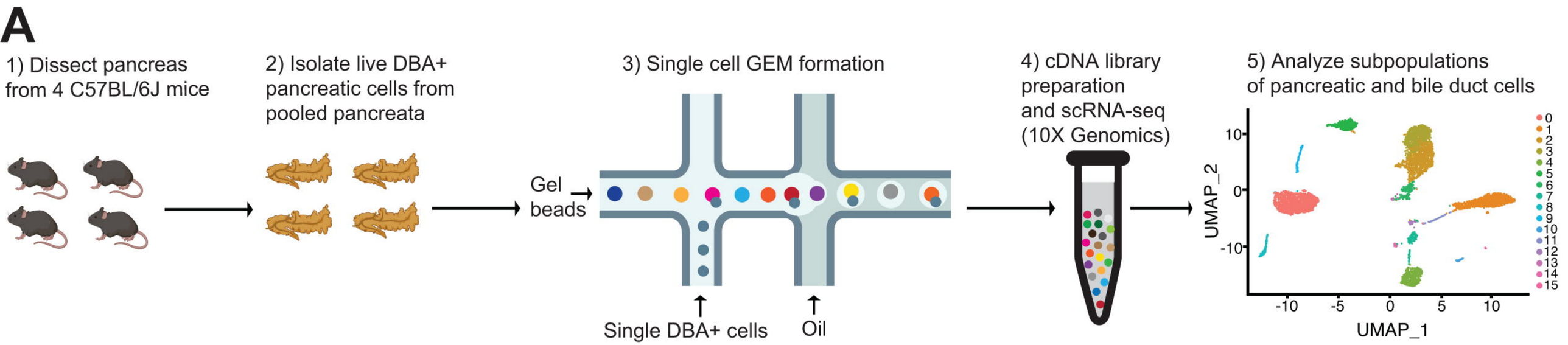

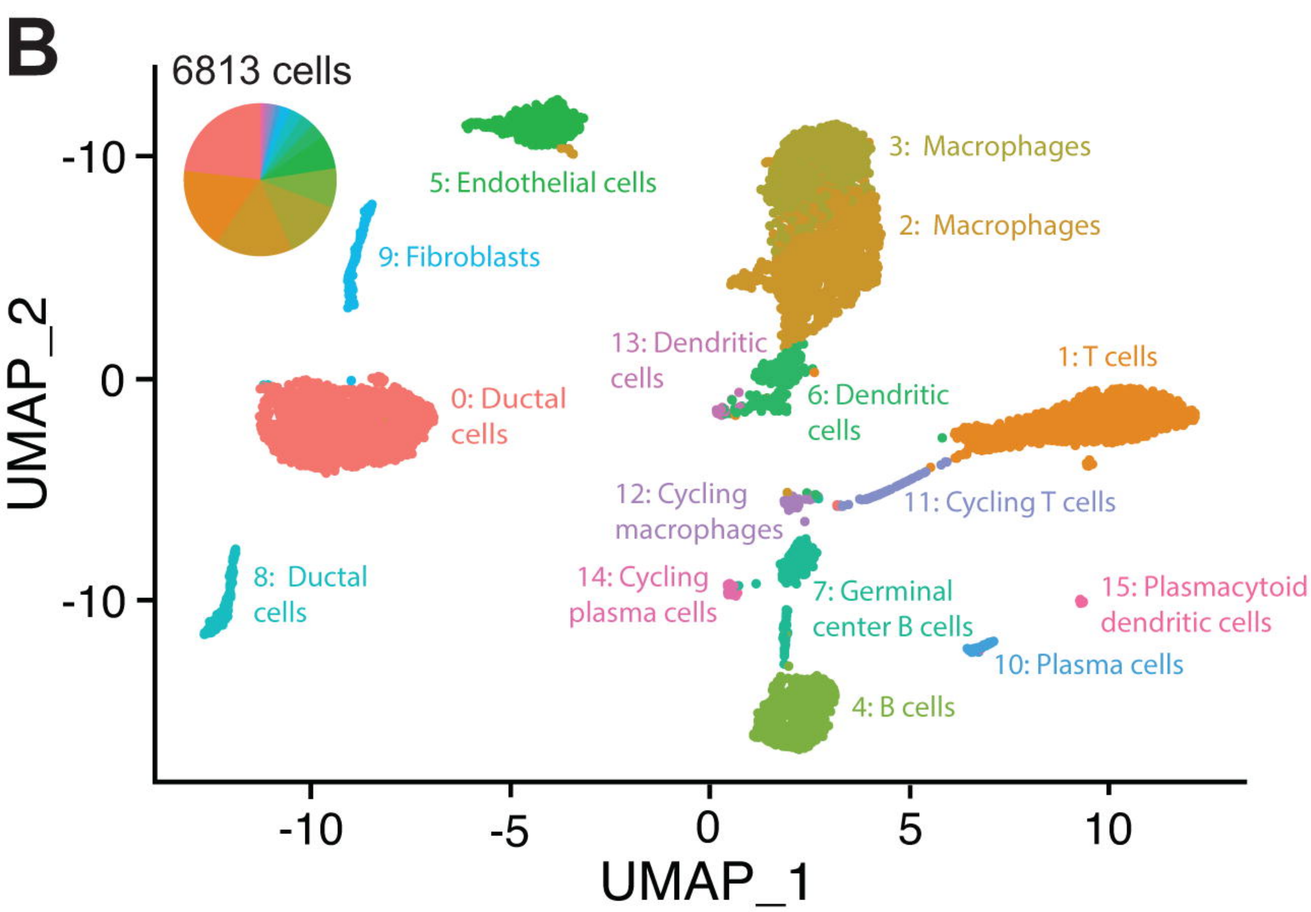

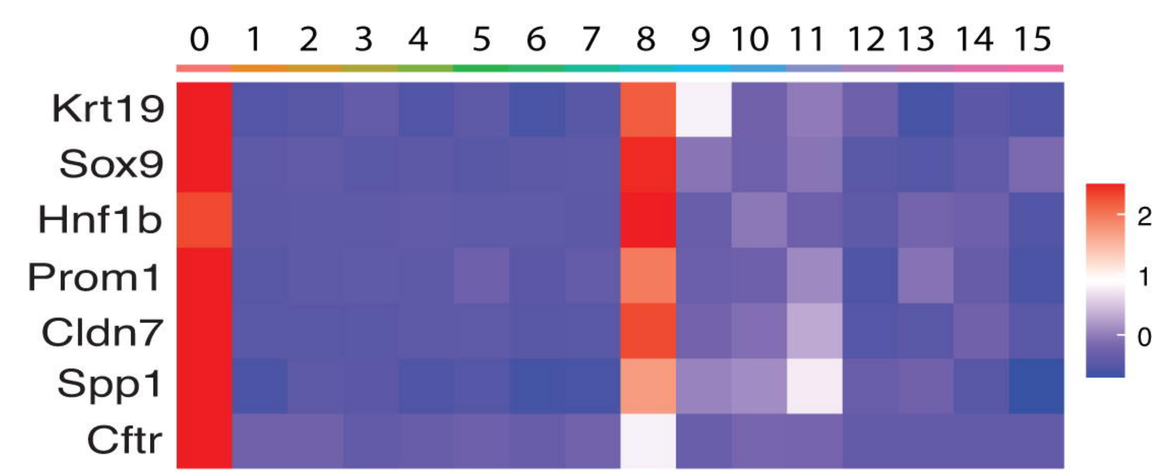

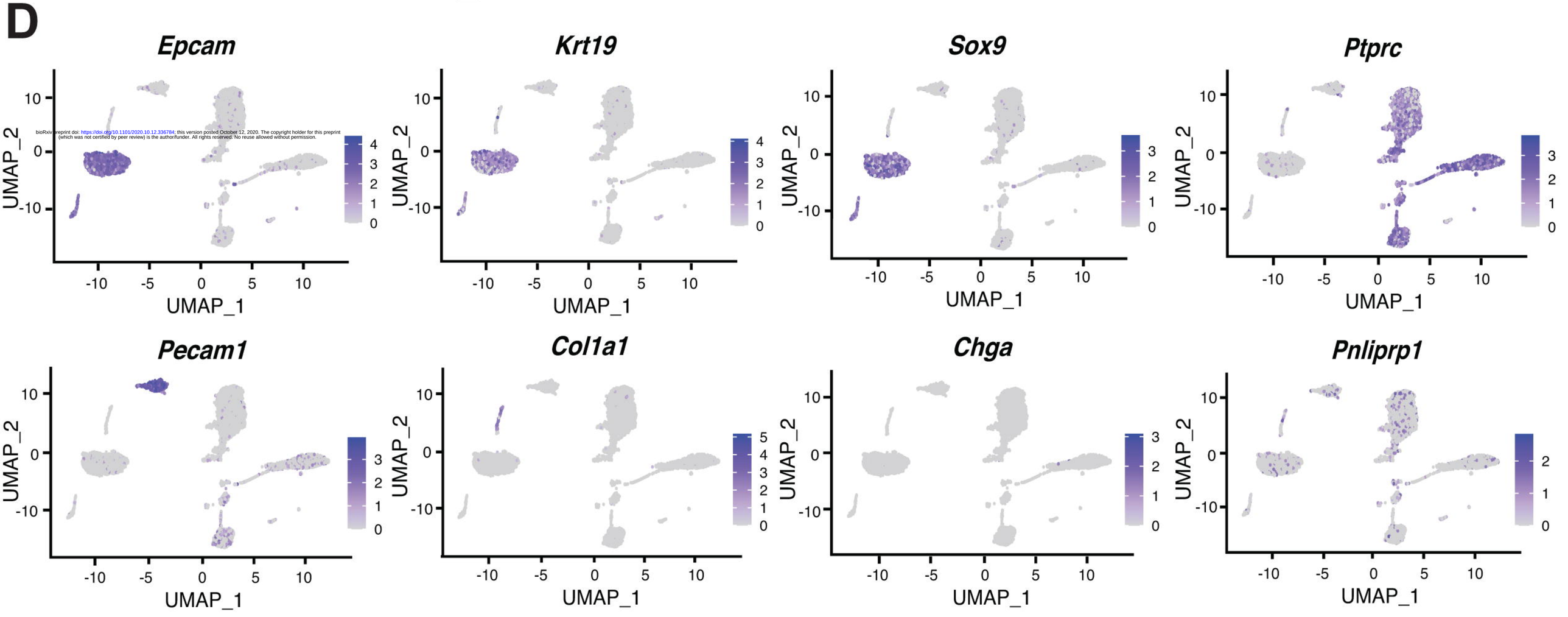

A

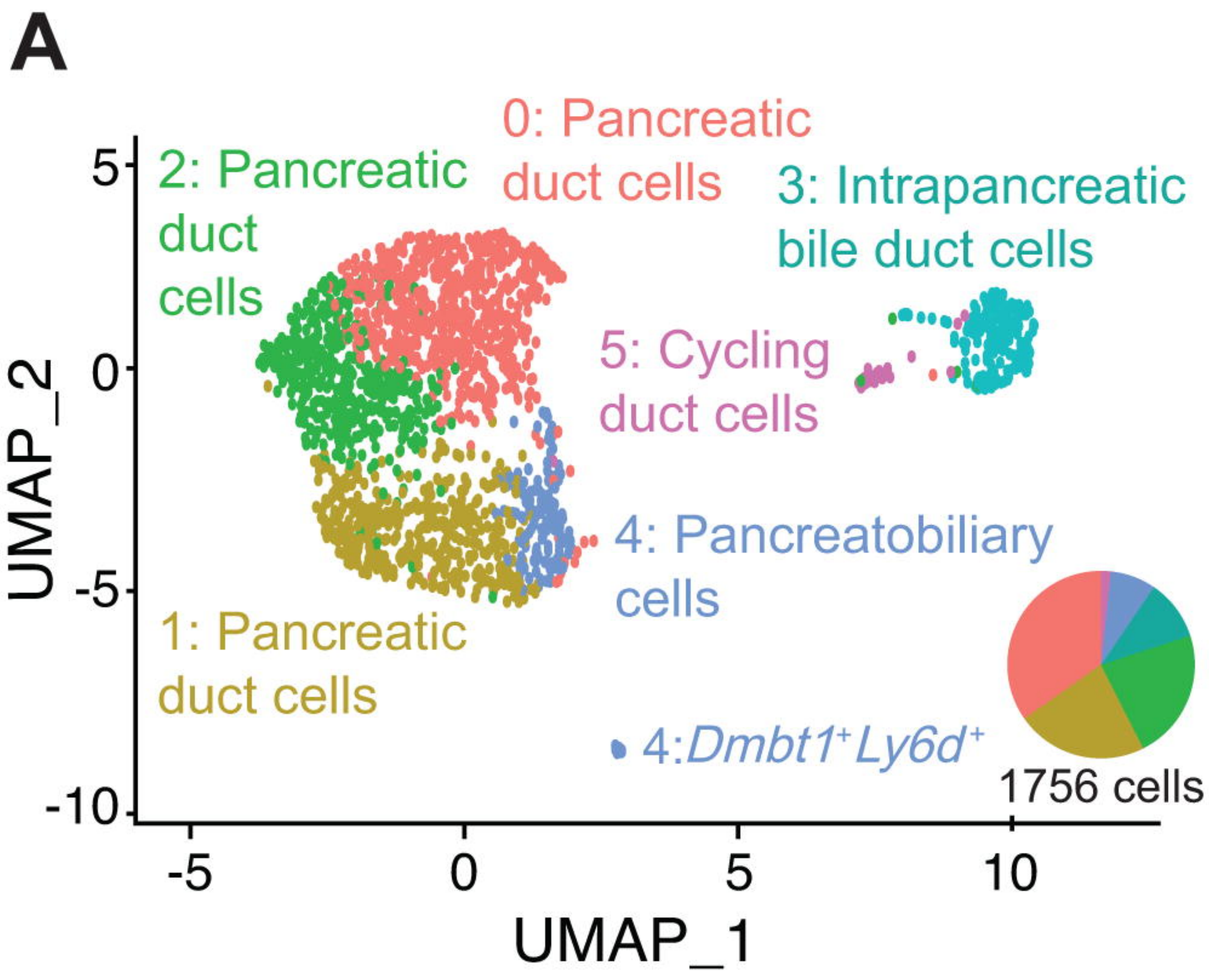

B

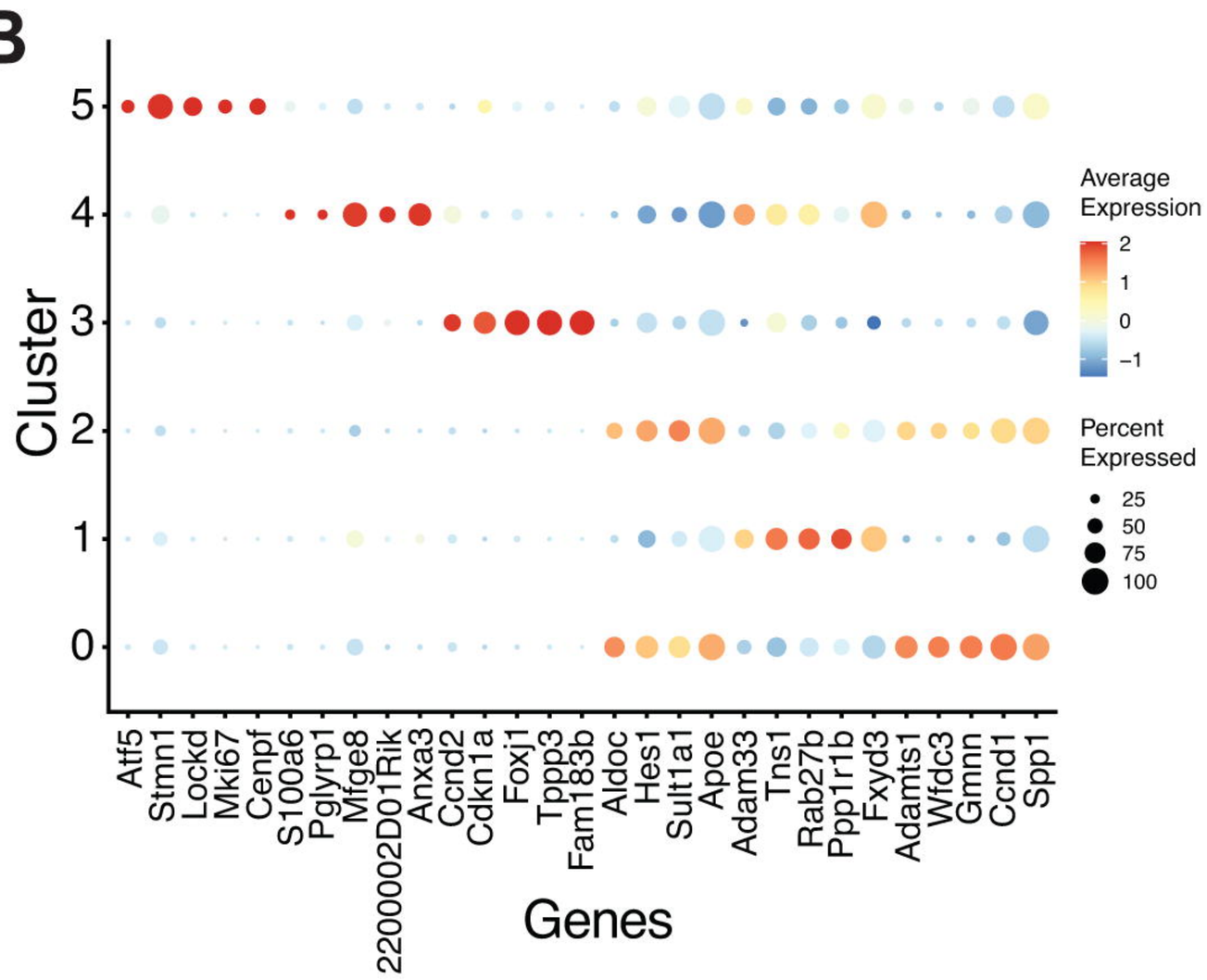

C

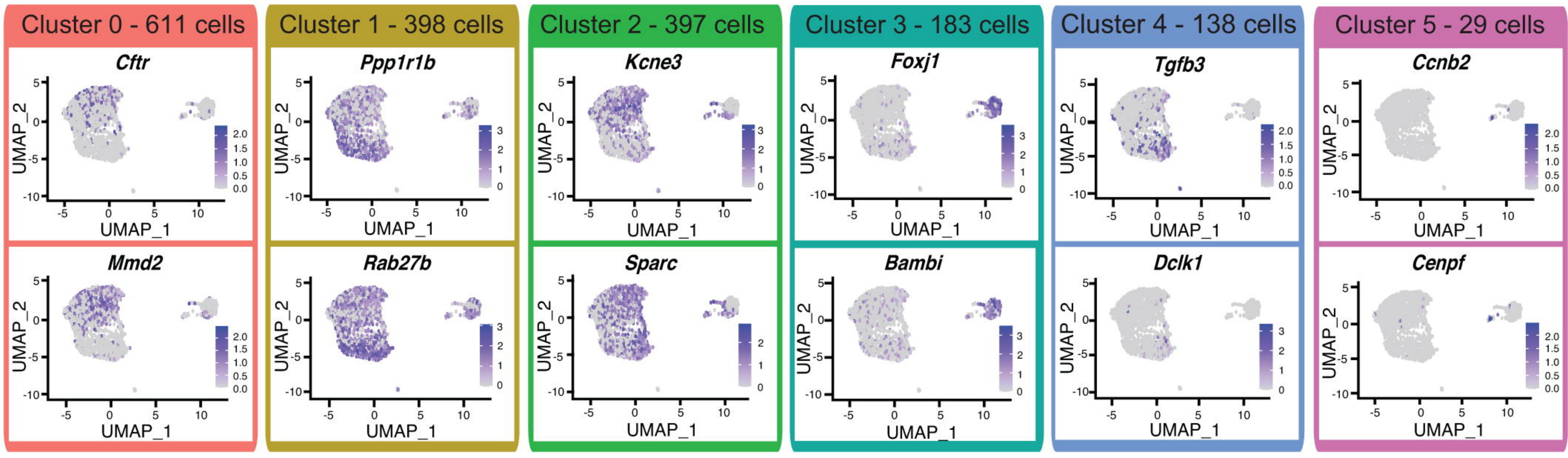

D

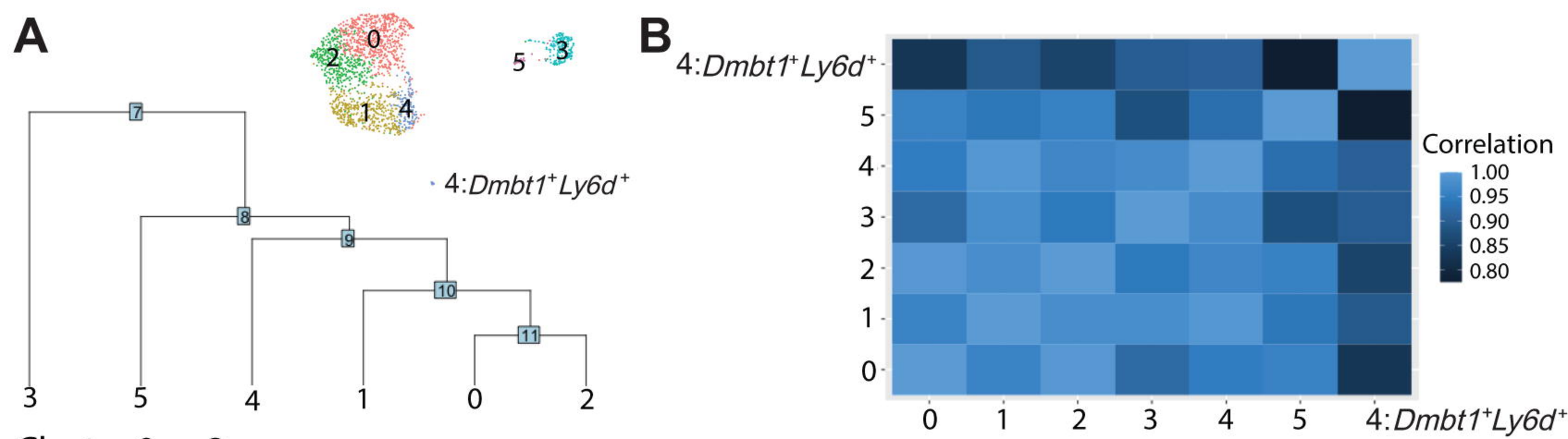

Cluster 0 vs 2

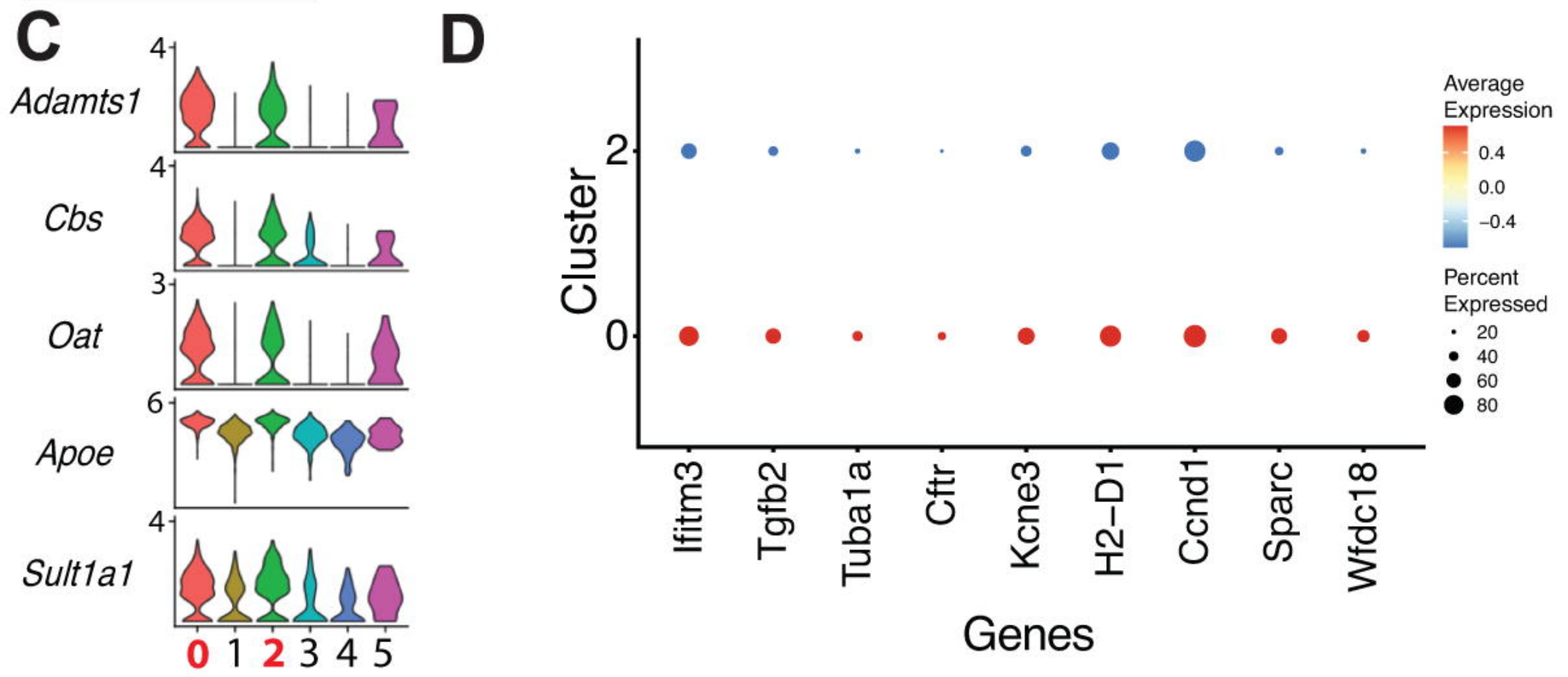

Cluster 4 vs 1

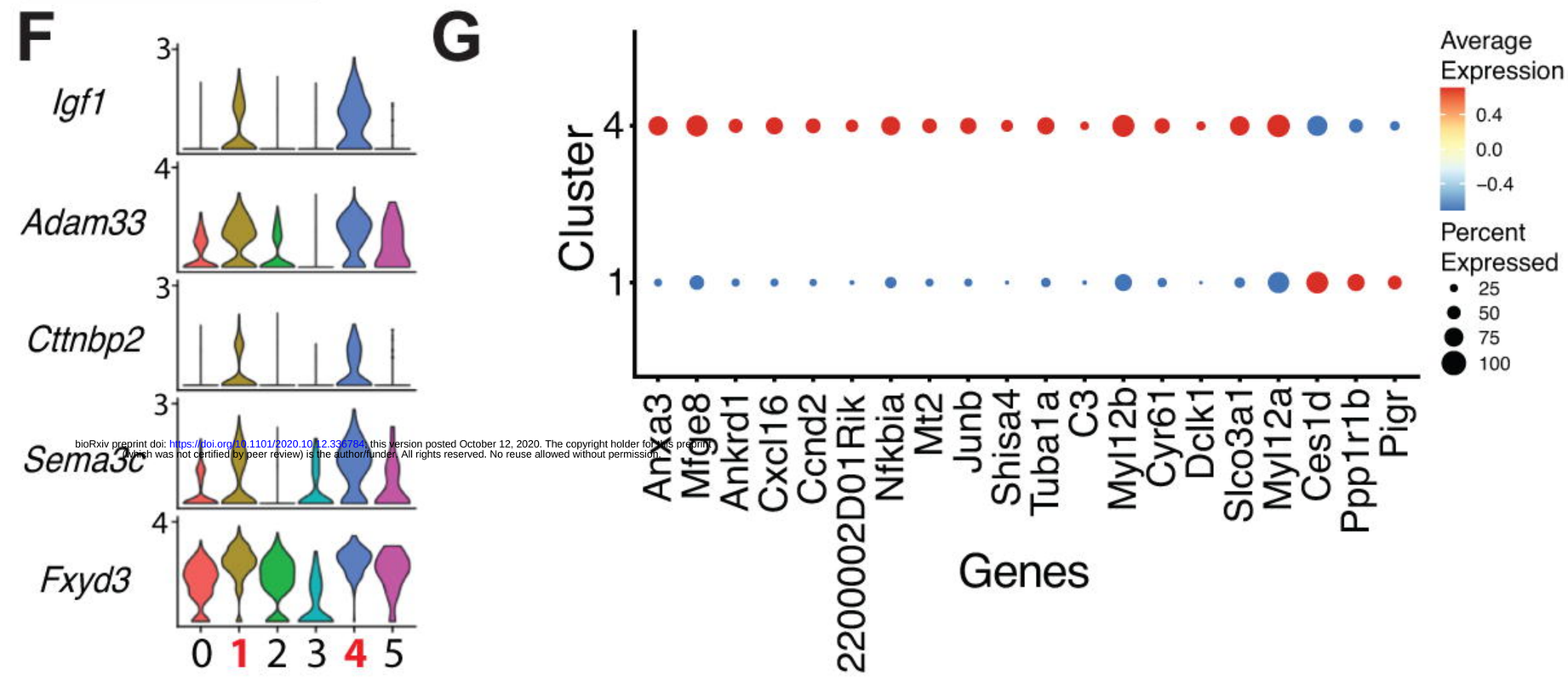

Cluster 4:*Dmbt1*$^+$*Ly6d*$^+$ vs Cluster 4

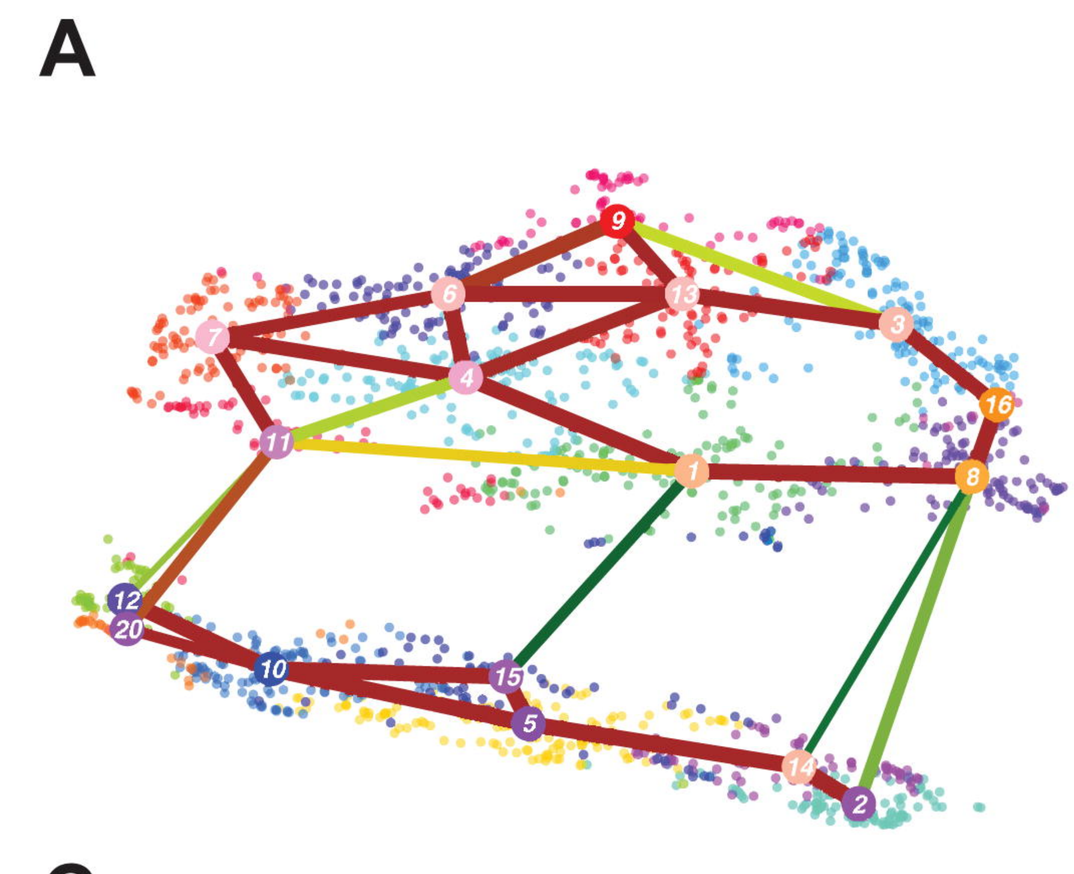

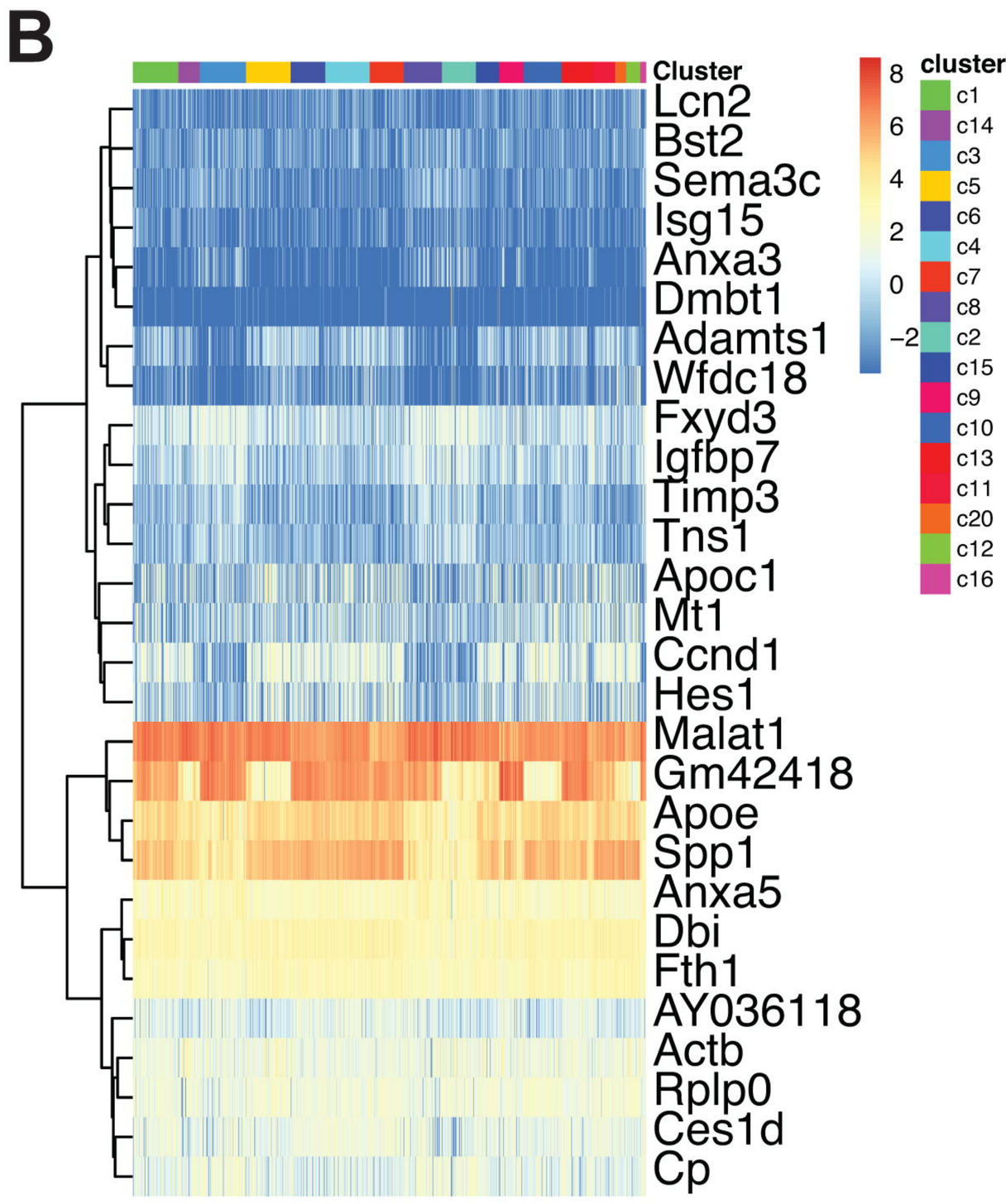

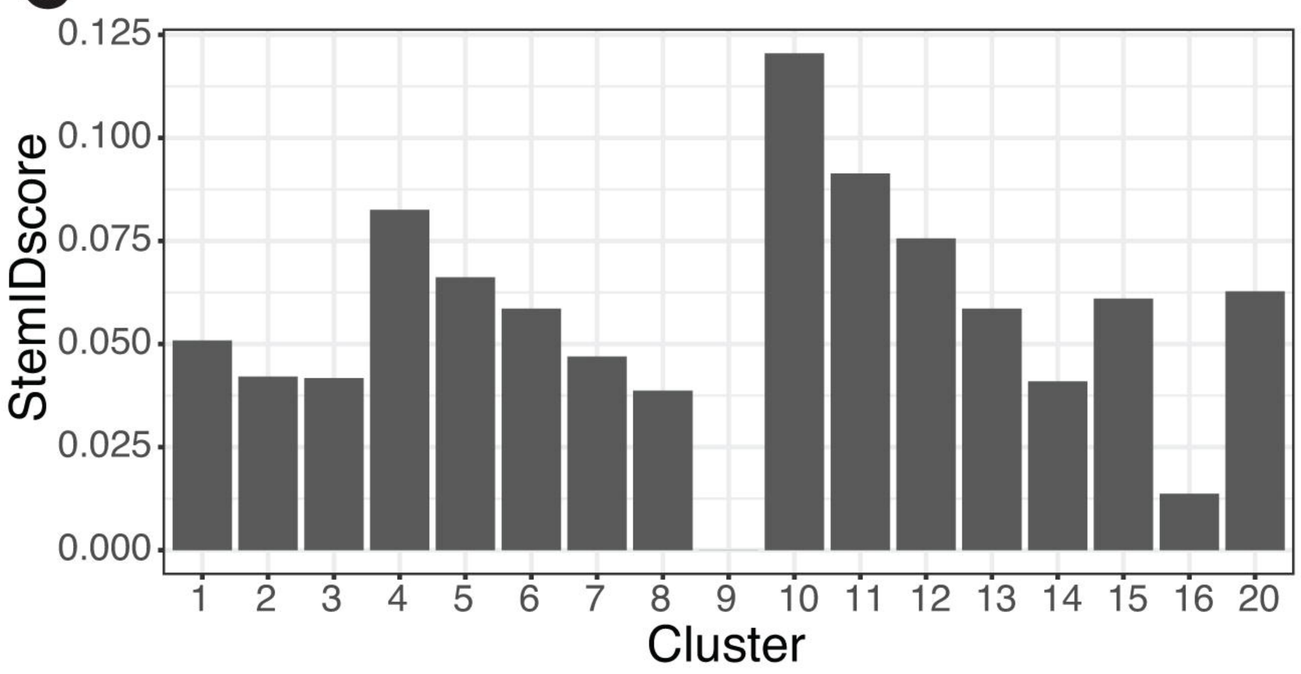

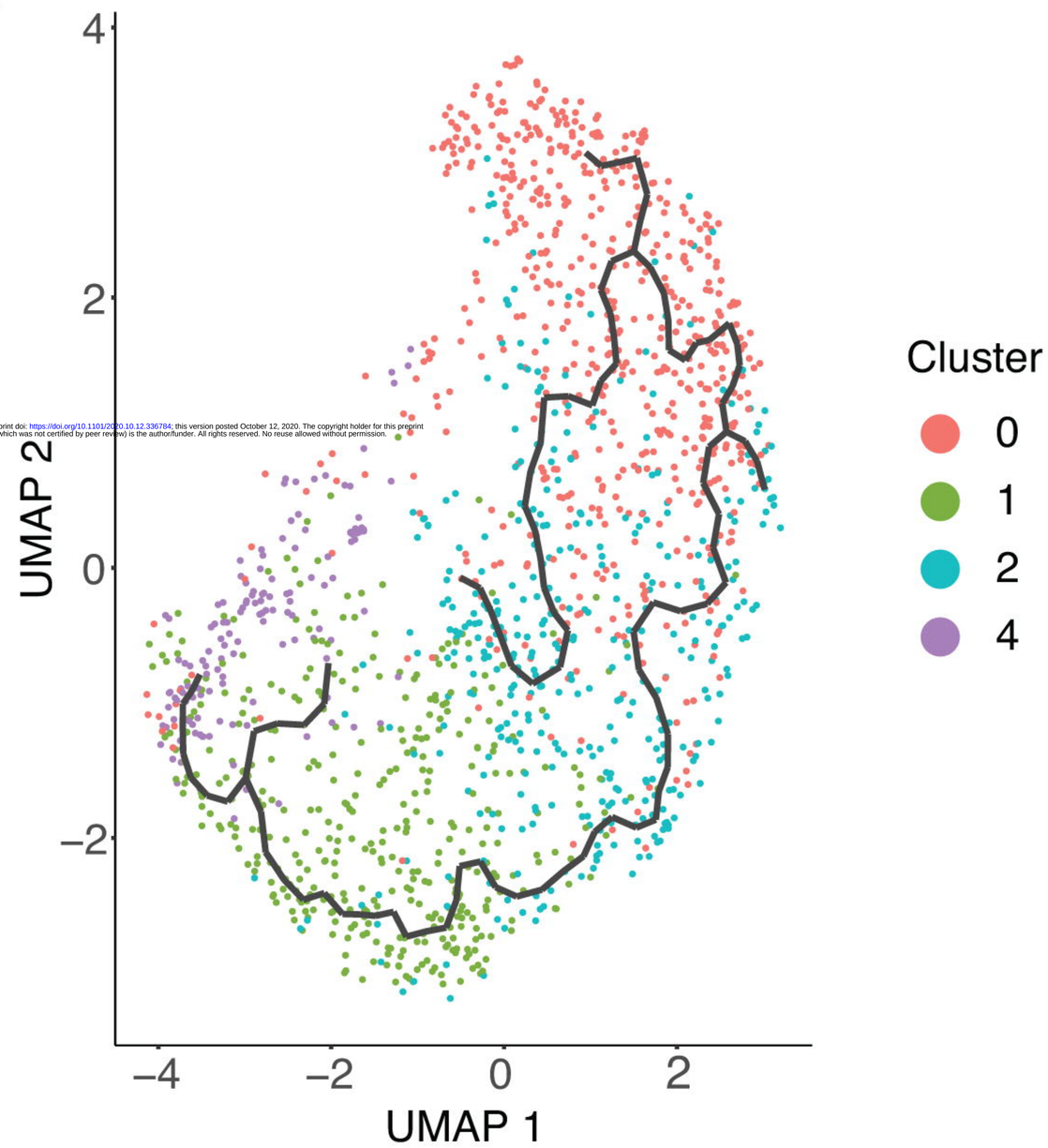

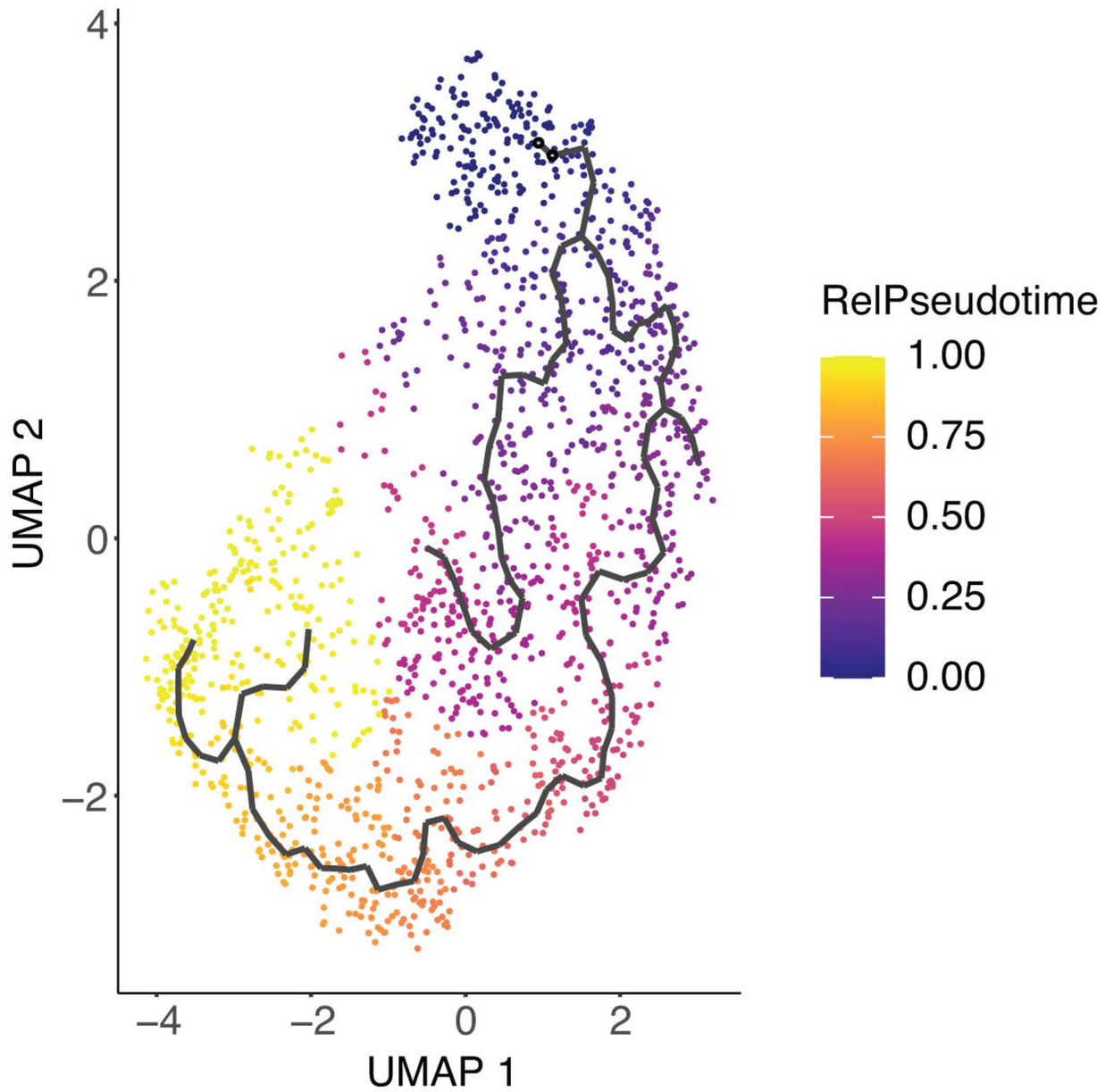

A

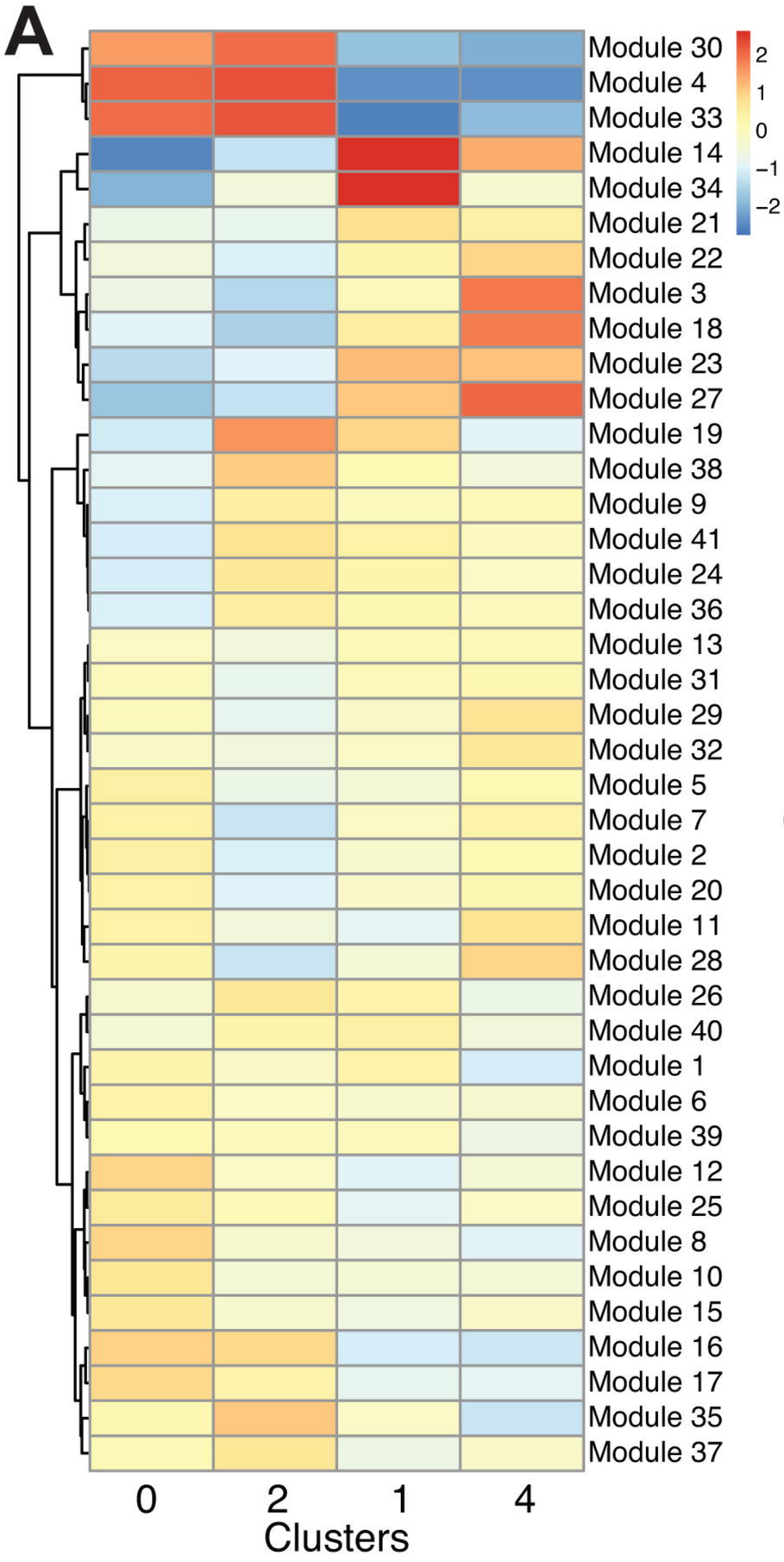

B

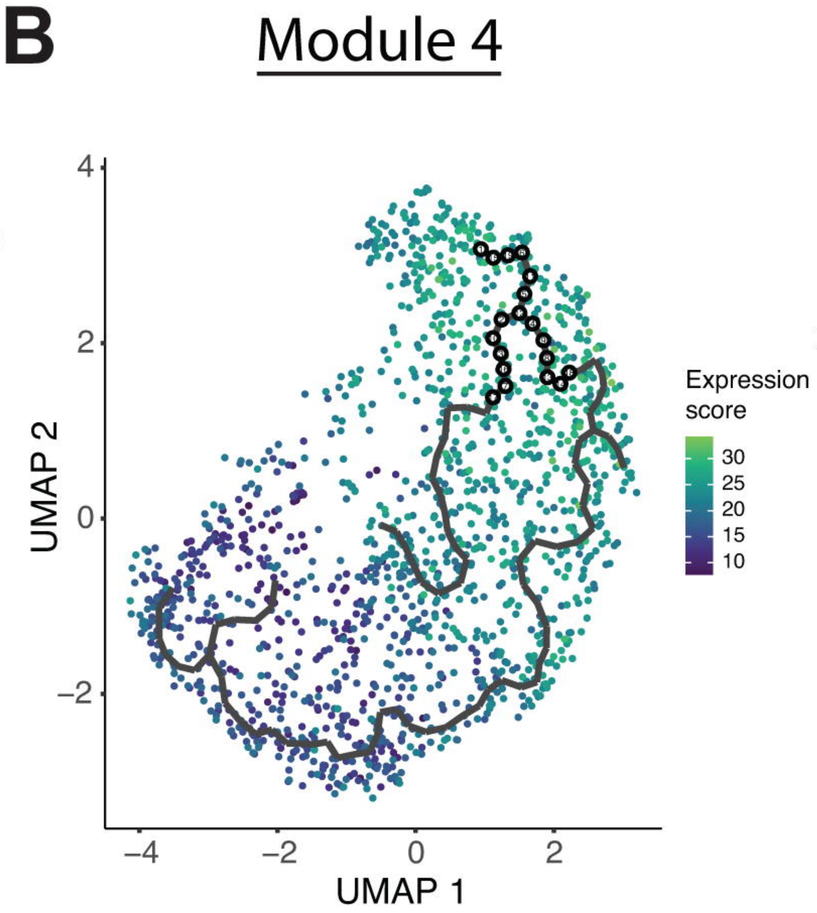

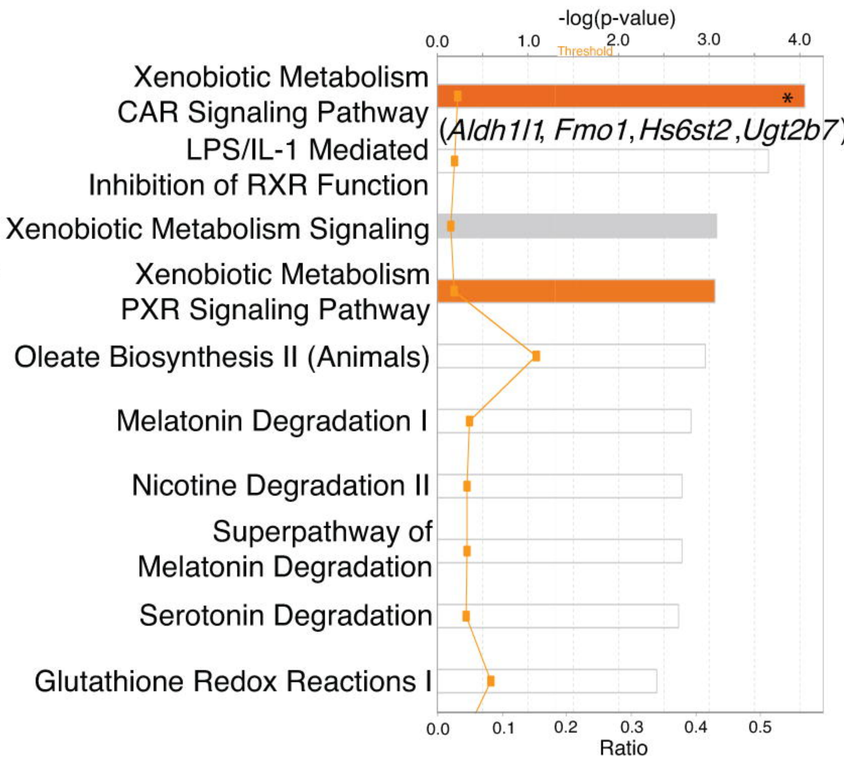

C

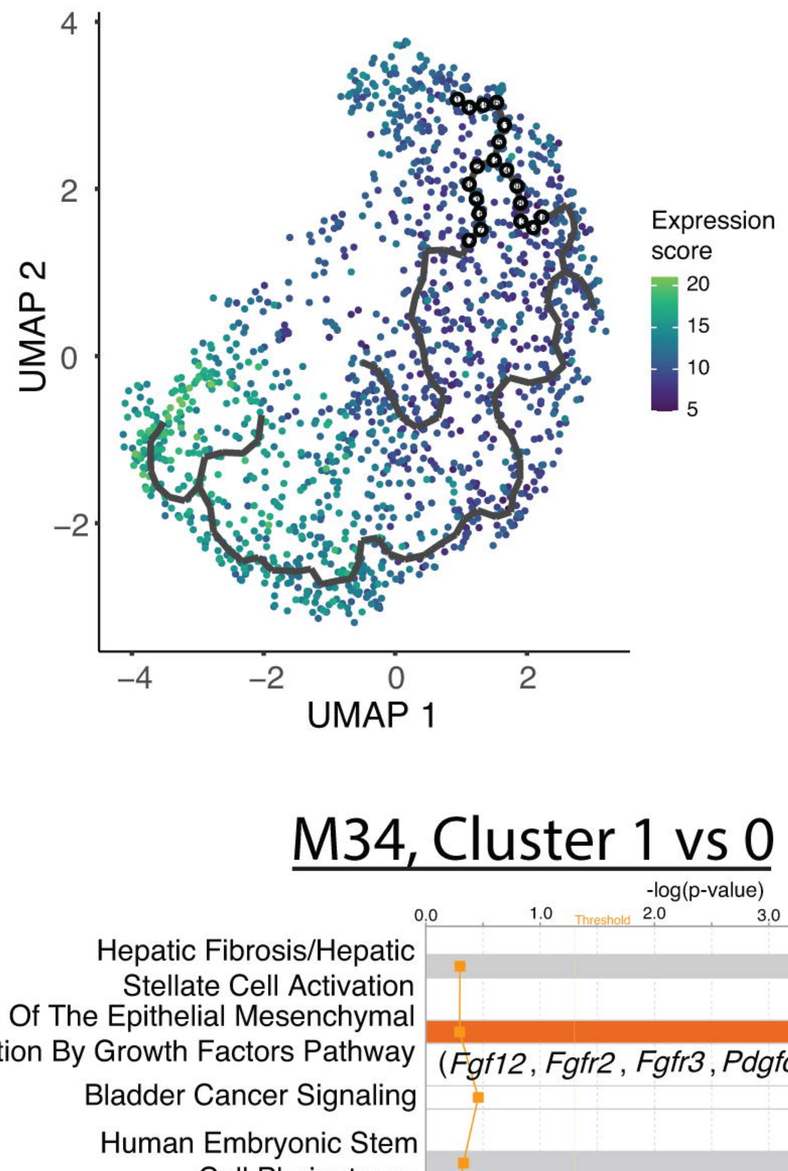

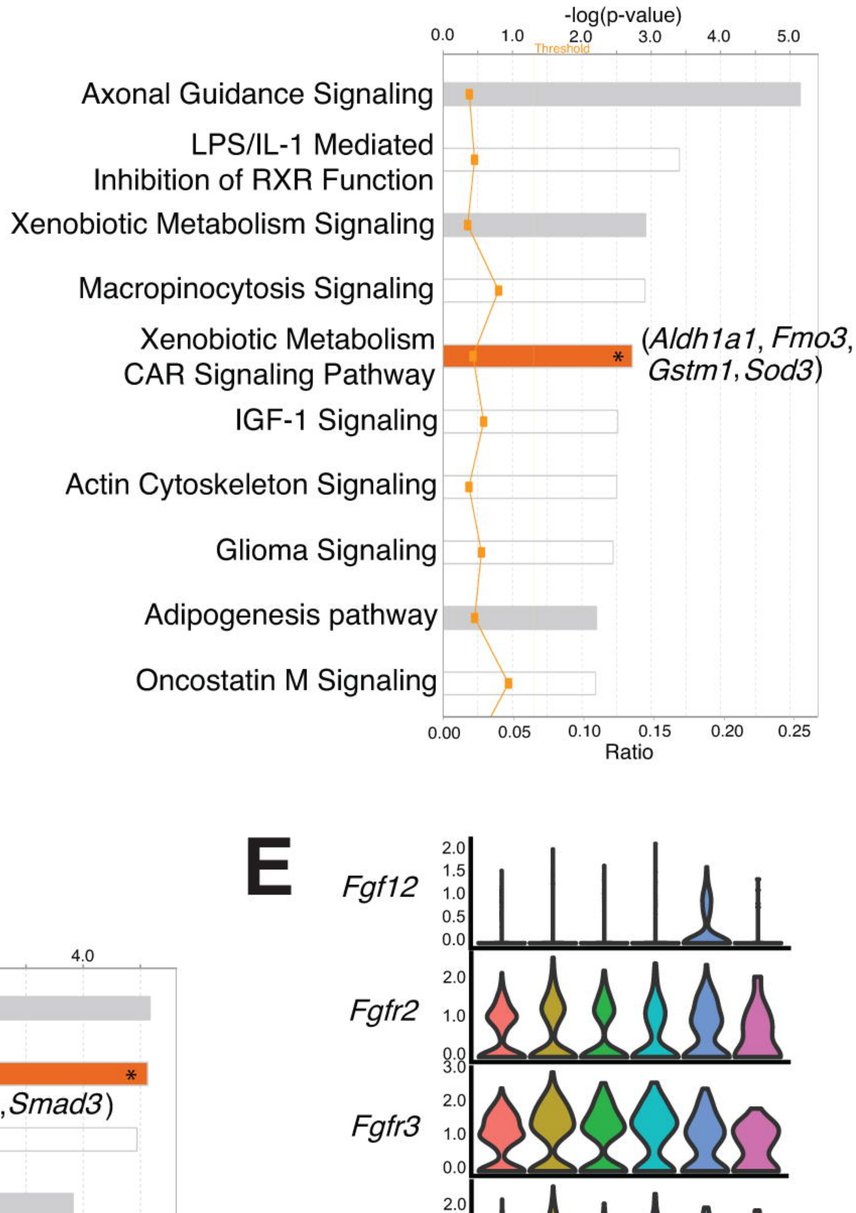

D

E

F

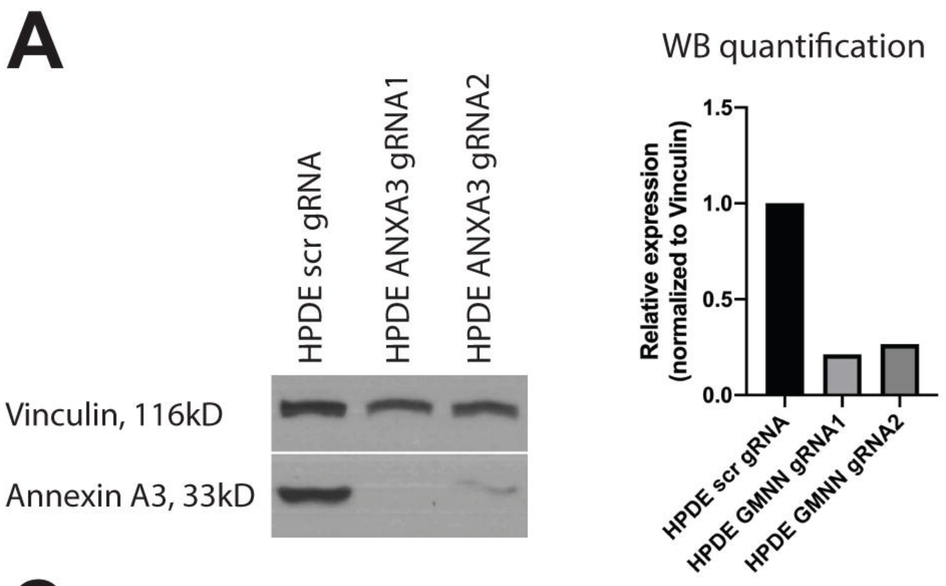

A
Normal
Chronic pancreatitis
Human
Ki67
Geminin
Dapi
CK19
B
Percent ductal cells
0.10
0.08
0.06
0.04
0.02
0.00
Normal
Chronic pancreatitis
Geminin+
Ki67+
C
0
1
2
3
4
5
Sox9+Hnf1b+
Sox9+
683
522
161
Hnf1b+
Tamoxifen administration
Hnf1bcreERT2Tg/wt; Geminin and
Sox9creERT2Tg/wt; Geminin mice
Pancreatic duct ligation or sham surgery
BrdU injection
Evaluation of Geminin loss in PDL model
7-9 weeks of age
≥ 48 hours post tamoxifen administration
24 and 4 hours before sacrifice
7 days and 30 days post surgery
D
Day 7
Percent ductal cells Geminin+
0.08
0.06
0.04
0.02
0.00
-0.02
Sham control
PDL Control
Sham Hnf1bcreERT2Tg/wt; Gemininf/f
PDL Hnf1bcreERT2Tg/wt; Gemininf/f
Sham Sox9creERT2Tg/wt; Gemininf/wt
PDL Sox9creERT2Tg/wt; Gemininf/wt
Sham Sox9creERT2Tg/wt; Gemininf/f
PDL Sox9creERT2Tg/wt; Gemininf/f
E
Sham Control
PDL Control
Sham Hnf1bTg/wt; Geminf/f
PDL Hnf1bTg/wt; Geminf/f
Sham Sox9Tg/wt; Geminf/wt
DBA
γ-H2AX
Day 7
PDL Sox9Tg/wt; Geminf/wt
Sham Sox9Tg/wt; Geminf/f
PDL Sox9Tg/wt; Geminf/f
F
Day 7
Average number of γ-H2AX+ foci per duct cell
Sham control
PDL Control
Sham Hnf1bcreERT2Tg/wt; Gemininf/f
PDL Hnf1bcreERT2Tg/wt; Gemininf/f
Sham Sox9creERT2Tg/wt; Gemininf/wt
PDL Sox9creERT2Tg/wt; Gemininf/wt
Sham Sox9creERT2Tg/wt; Gemininf/f
PDL Sox9creERT2Tg/wt; Gemininf/f
G
Sham Control
PDL Control
Sham Sox9Tg/wt; Geminf/f
PDL Sox9Tg/wt; Geminf/f
DBA
γ-H2AX
Day 30
H
Day 30
Average number of γ-H2AX+ foci per duct cell
Sham control
Control
Sham Sox9creERT2Tg/wt; Geminf/f
PDL Sox9creERT2Tg/wt; Geminf/f